3D MXene Architectures for Efficient Energy Storage and Conversion

Ke Li, Meiying Liang, Hao Wang, Xuehang Wang, Yanshan Huang, João Coelho, Sergio Pinilla, Yonglai Zhang, Fangwei Qi, Valeria Nicolosi,* and Yuxi Xu*

2D transition metal carbides and/or nitrides (MXenes), by virtue of high electrical conductivity, abundant surface functional groups and excellent dispersion in various solvents, are attracting increasing attention and showing competitive performance in energy storage and conversion applications. However, like other 2D materials, MXene nanosheets incline to stack together via van der Waals interactions, which lead to limited number of active sites, sluggish ionic kinetics, and finally ordinary performance of MXene materials/devices. Constructing 2D MXene nanosheets into 3D architectures has been proven to be an effective strategy to reduce restacking, thus providing larger specific surface area, higher porosity, and shorter ion and mass transport distance over normal 1D and 2D structures. In this review, the commonly used strategies for manufacturing 3D MXene architectures (3D MXenes and 3D MXene-based composites) are summarized, such as template, assembly, 3D printing, and other methods. Special attention is also given to the structure–property relationships of 3D MXene architectures and their applications in electrochemical energy storage and conversion, including supercapacitors, rechargeable batteries, and electrocatalysis. Finally, the authors propose a brief perspective on future opportunities and challenges for 3D MXene architectures/devices.

1. Introduction

The successful exfoliation of graphene in 2004 aroused tremendous research interest in 2D nanomaterials.[1] Due to their unusual electrical, mechanical, and optical properties, 2D nanomaterials show great potential for extensive applications in optoelectronics, biology, medicine, environmental protection, catalysis, sensors, energy storage, and conversion.[2] Thus, new 2D nanomaterials, such as hexagonal boron nitrides,[3] transition metal dichalcogenides,[4] silicene,[5] phosphorene,[6] germanane,[7] and metal oxides,[8] have been successfully prepared as well.

MXenes, an emerging family of 2D transitional metal carbides and/or nitrides with a general formula of $M_{n+1}X_nT_x$, are obtained by selective etching of A elements from ternary MAX phases ($M_{n+1}AX_n$), where M is an early transition metal (Sc, Ti, V, Cr, Zr, Nb, Mo, Hf, or Ta), A is a group IIIA or IVA species, X is carbon and/or nitrogen, n is an integer between 1 and 4, and T_x represents surface functional groups.[9] The unique structure of MXenes renders them particularly attractive for electrochemical energy storage and conversion applications because: 1) the transition metal carbide core enables metallic conductivity (up to 10 000 S cm^{-1} for $Ti_3C_2T_x$) for fast electrons transport throughout the electrodes;[10] 2) the transition metal oxide-like surface is redox-active;[11] and 3) the negatively charged surface groups (—O, —OH, and —F)

Dr. K. Li, Dr. Y. Zhang, Prof. Y. Xu
School of Engineering
Westlake University
Hangzhou, Zhejiang Province 310024, China
E-mail: xuyuxi@westlake.edu.cn

Dr. K. Li, Dr. Y. Zhang, Prof. Y. Xu
Institute of Advanced Technology
Westlake Institute for Advanced Study
Hangzhou, Zhejiang Province 310024, China

Dr. K. Li, M. Liang, Dr. J. Coelho, Dr. S. Pinilla, Prof. V. Nicolosi
School of Chemistry
Centre for Research on Adaptive Nanostructures and Nanodevices
(CRANN) & Advanced Materials Bio-Engineering Research Centre (AMBER)
Trinity College Dublin
Dublin 2, Ireland
E-mail: nicolov@tcd.ie

Dr. H. Wang
School of Chemical and Biomedical Engineering
Nanyang Technological University
50 Nanyang Avenue, Singapore 639798, Singapore

Dr. X. Wang
A. J. Drexel Nanomaterials Institute and Department of Materials
Science and Engineering
Drexel University
Philadelphia, PA 19104, USA

Dr. Y. Huang
School of Chemical and Environmental Engineering
Shanghai Institute of Technology
Shanghai 201418, China

Dr. F. Qi
Institute of Bioadditive Manufacturing
Jiangxi University of Science and Technology
Nanchang 330013, China

supply abundant sites for active catalysts anchoring.[12] For example, a $Ti_3C_2T_x$ hydrogel delivered an ultrahigh volumetric capacitance of 1500 F cm^{-3},[11] $MoS_2/Ti_3C_2T_x$@C hybrids with uniform growth of MoS_2 nanoplates on MXene nanosheets showed excellent activity and durability in an acidic solution for hydrogen evolution reaction (HER).[13] Nevertheless, aggregation and self-restacking of single or few-layer MXene nanosheets are usually inevitable during the electrode fabrication processes due to strong van der Waals interactions and hydrogen bonds between adjacent nanosheets. These processes limit electrolyte ions accessibility, hindering the full utilization of the functional surfaces of MXenes, thus impairing their electrochemical performance.[14]

The construction of 3D architectures from 2D MXenes provides an effective strategy to overcome these issues.[15] Generally, 3D MXene architectures possess the following advantages: 1) the large specific surface area of MXene nanosheets can be maintained in a 3D MXene architectures as the restacking of nanosheets is effectively inhibited.[16] Therefore, a great number of electrochemically active sites are exposed to electrolyte, thus enabling sufficient electrochemical reactions; 2) the rich channels in 3D MXene architectures are favorable for rapid diffusion of electrolyte, and the outstanding electrical conductivity of MXenes makes them ideal active materials or current collectors for fast transport of charge carriers within the porous framework; 3) the abundant functional groups (O, −OH, and −F) can serve as appealing sites for binding various organic or inorganic species, which provides an opportunity for the construction of 3D MXene architectures with diverse complexity and functionality; 4) for practical applications, the 3D conductive architectures ensure efficient charge transport throughout the bulk volume of thick electrodes, which is desirable for maximizing the utilization of active materials regardless of electrode thickness or mass loading. Not surprisingly, 3D MXene architectures are very promising for high-performance energy storage and conversion applications.

In this review, we first highlight the commonly employed fabrication methods for the construction of 3D MXene architectures. Then, their applications in electrochemical energy
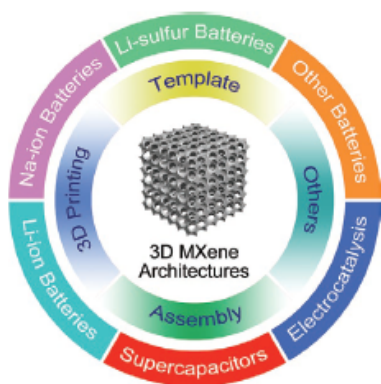
Ke Li is currently a postdoctoral researcher at Trinity College Dublin, Ireland. He received his Ph.D. in Chemistry and Physics of Polymers from Fudan University, China in 2019. He worked as a visiting researcher in A. J. Drexel Nanomaterials Institute, Drexel University, Philadelphia, USA from 2017 to 2018. His research interests focus on 2D materials and their applications in energy storage and conversion.

Valeria Nicolosi is an ERC Research Professor of the School of Chemistry and the School of Physics at Trinity College Dublin. She received B.Sc. from the University of Catania (Italy) in 2001 and Ph.D. from Trinity College Dublin (Ireland) in 2006. She moved to the University of Oxford (UK) in 2008 as a Marie Curie Fellow. Her research group works on the processing and cutting-edge electron microscopy characterization of low-dimensional nanomaterials, and their energy storage applications.

Yuxi Xu received his B.S. degree from Wuhan University (2007) and Ph.D. degree from Tsinghua University (2011), China. He then worked as a postdoctoral fellow at University of California, Los Angeles, USA. He joined the faculty of Fudan University in 2015 and moved to Westlake University, Hangzhou, China in 2019. His research interests include chemically modified graphene, 2D polymers, and self-assembled functional materials.

Figure 1. Schematic of various fabrication strategies for preparing 3D MXene architectures, including template, assembly, 3D printing, among other methods, along with their applications in supercapacitors, rechargeable batteries (Li-ion, Na-ion, and Li–S batteries) and electrocatalysis.

storage and conversion are discussed, with special focus in supercapacitors, rechargeable batteries, and electrocatalysis (**Figure 1**). Finally, we list some challenges and opportunities in this promising research area. We also suggest how these problems might be solved to further push forward the advancement of 3D MXene architectures for greater breakthroughs and a broader range of applications.
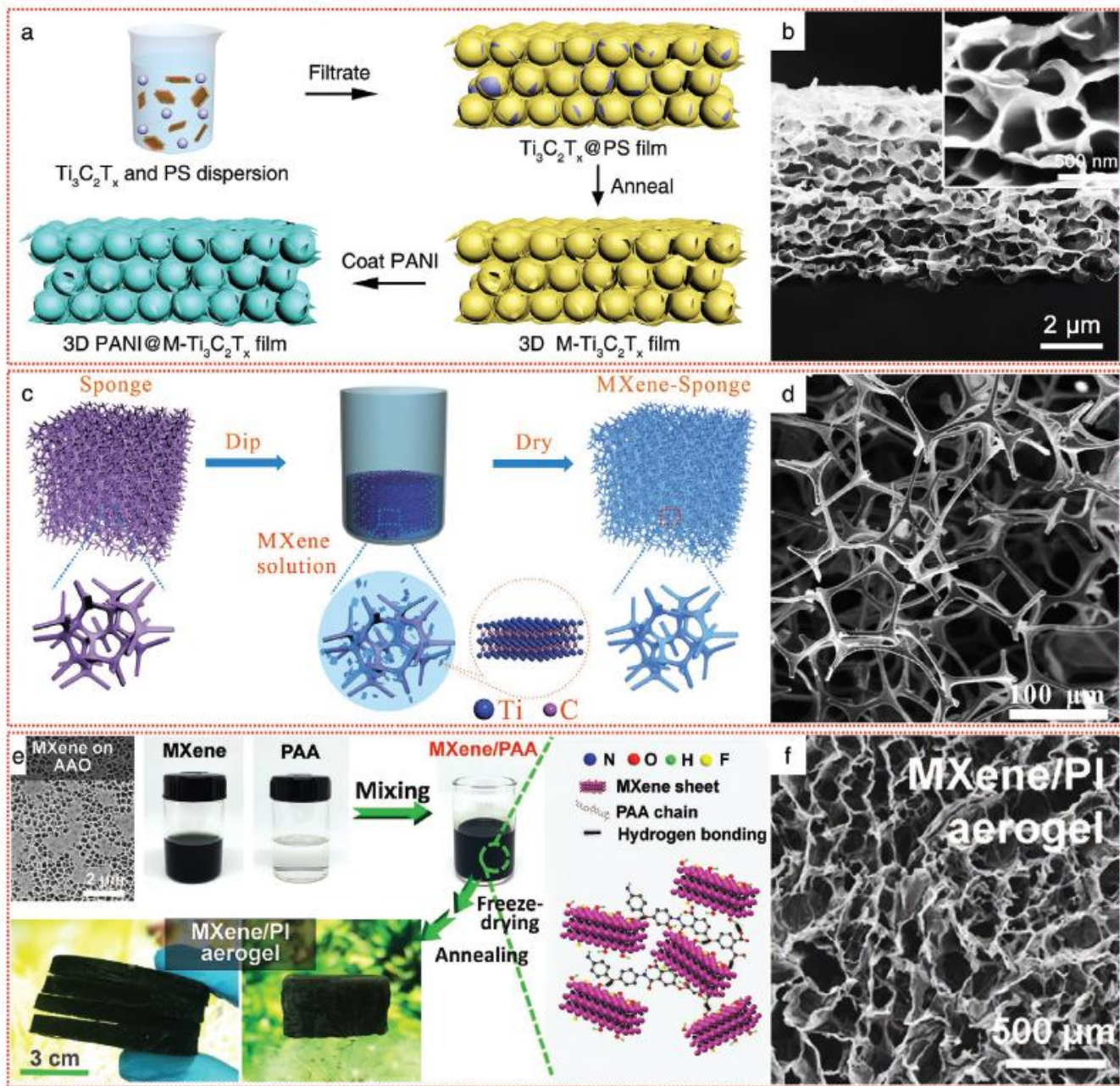
Figure 2. Template methods for manufacturing 3D MXene architectures. a) Schematic of the construction of 3D macroporous PANI@M-Ti$_3$C$_2$T$_x$ frameworks with PS spheres as template. b) SEM images of the 3D PANI@M–Ti$_3$C$_2$T$_x$ film. Reproduced with permission.[15a] Copyright 2019, Wiley-VCH. c) Schematic illustration of the fabrication procedure of MXene-sponge. d) SEM image of the MXene-sponge. Reproduced with permission.[27a] Copyright 2018, Elsevier Ltd. e) Schematic diagrams of the fabrication process and digital images showing the light weight of the MXene/PI aerogel, which can rest on the top of a dandelion. f) SEM image of the MXene/PI aerogel. Reproduced with permission.[32a] Copyright 2018, Wiley-VCH.

2. Manufacturing Strategies for 3D MXene Architectures

As the preparation methods of MXenes have been insightfully summarized elsewhere,[9f,17] here we only focus on the fabrication strategies for 3D MXene architectures. These routes mainly include template, assembly, 3D printing, among other methods.

2.1. Template Method

Template synthesis is one of the most straightforward and effective methods for manufacturing 3D porous architectures.[18] In addition, the microstructure of the resultant 3D materials can be easily customized by adjusting the size and/or morphology of templates.[19] In general, the templated synthesis of 3D materials includes the following steps: 1) template preparation;

2) coating desired materials on the selected template; and 3) template removal (if necessary).[20]

Polystyrene (PS) and poly(methyl methacrylate) (PMMA) spheres are the most widely employed templates for constructing 3D graphene materials, which also applies to build 3D macroporous MXenes.[11,15a,21] In a typical example (**Figure 2**a), PS spheres and $Ti_3C_2T_x$ MXene with a mass ratio of 3:1 were first homogeneously mixed in aqueous solution. Throughout this process, MXene nanosheets wrapped the surface of PS spheres spontaneously because of the interaction between their surface hydroxyl groups. Afterward, a 3D $Ti_3C_2T_x$ MXene film was obtained by filtrating the mixed dispersion, followed by the removal of PS spheres at 450 °C in argon gas. In this process, due to the van der Waals interactions and hydrogen bonds between neighboring 2D $Ti_3C_2T_x$ nanosheets, the porous architecture of 3D MXene frameworks remained unchanged after template removal.[15a] These films could be further used as porous substrates for manufacturing 3D MXene-based nanocomposites, such as the 3D polyaniline@macroporous $Ti_3C_2T_x$ (3D PANI@M-$Ti_3C_2T_x$) as shown in Figure 2b.[15a] Melamine formaldehyde spheres[22] and sulfur particles[23] were also used as templates for preparing 3D MXene architectures in a similar process.

3D monoliths with porous structure can also be directly used as templates for producing 3D MXene architectures, without the filtration process. Nickel foam,[24] melamine foam,[25] carbon foam,[26] commercial sponge,[27] graphene aerogel,[28] and electrospun polymer fiber networks[29] are commonly used templates. In this case, MXenes are directly coated onto the skeletons of 3D templates by a facile dipping or dropping method. Taken the MXene–sponge composite as an example, the clean melamine sponge-substrate was first soaked in MXene solution to absorb 2D nanosheets, followed by transferring into a vacuum oven at 80 °C for drying. After 24 h, a 3D MXene–sponge composite formed with a thin layer of MXenes anchoring on the 3D skeleton of the sponge (Figure 2c,d).[27a]

Due to the hydrophilic nature of MXene nanosheets, freeze-drying can also lead to the formation of macroporous MXenes with ice crystals as templates.[30] Typically, to produce a 3D porous MXene monolith, the $Ti_3C_2T_x$ aqueous dispersion is initially frozen in a dry ice bath, followed by freeze-drying at −70 °C for 48 h to remove the ice templates.[30a] Scanning electron microscope (SEM) images showed that the 3D $Ti_3C_2T_x$ MXene monolith has a macroporous structure, with a pore size around 20 µm and slightly corrugated cell walls. It was proposed that during freeze casting, MXene nanosheets were repulsed by the growing ice crystals getting entrapped at their boundaries, yielding a continuous network. To further prevent the self-stacking of MXene nanosheets and enhance the mechanical strength of the resultant 3D architectures, reduced graphene oxide (rGO)[30i,31] and polyimide (PI)[32] were introduced. For instance, after incorporating PI (Figure 2e,f),[32a] the characteristic (002) peak slightly shifted from 6.40° ($Ti_3C_2T_x$ MXene) to 6.01° (3D MXene/PI aerogel), which implies an enlarged interlayer spacing from 1.38 to 1.47 nm. This effect suggests that the intercalation of PI into the MXene galleries successfully disrupted their restacking tendency. Moreover, the synergistic effect between MXene and PI endowed the 3D aerogel remarkable flexibility to bear deformations of 80% compression, torsion, and even 180° bending. This ice-template method was

also employed to prepare several other 3D MXene architectures for different applications, examples are 3D $Ti_3C_2T_x$/carbon for wearable sensors,[33] 3D $Ti_3C_2T_x$/polyethylene glycol[34] and 3D $Ti_3C_2T_x$/bacterial cellulose/polyethylene glycol[35] for solar energy storage and conversion, 3D Co_3O_4/$Ti_3C_2T_x$/rGO,[36] 3D NiO/$Ti_3C_2T_x$,[37] and 3D Fe_2O_3/$Ti_3C_2T_x$[38] for electrochemical energy storage.

2.2. Assembly Method

As MXenes have abundant surface groups (−O, −OH, and −F), they can be uniformly dispersed in aqueous solution. By introducing gelation agents or disrupting the balance between the electrostatic repulsion force and the Van der Waals interactions, 2D MXene nanosheets in solution will interconnect and assembly into 3D porous architectures.[39]

Graphene oxide (GO), a typical gelation agent, can mix homogeneously with MXene nanosheets in water and lead to the formation of 3D MXene/rGO composites.[40] For instance, rGO sheets resulting from the reduction of GO by ascorbic acid and hydrothermal treatment interconnected with each other and formed a 3D framework. Meanwhile, $Ti_3C_2T_x$ nanosheets were assembled onto the surfaces of the rGO framework, leading to the formation of a $Ti_3C_2T_x$/rGO hybrid hydrogel (**Figure 3**a).[40a] The resulting $Ti_3C_2T_x$/rGO hybrid aerogel showed a uniform and overall aligned cellular structure with a unidirectional assembly of rGO and $Ti_3C_2T_x$ nanosheets (Figure 3b). This porous and aligned structure allowed the $Ti_3C_2T_x$/rGO aerogel to stand on a flower. 100 mg of $Ti_3C_2T_x$/rGO aerogel was shown to withstand a load of 500 g without fracturing, thus revealing a good mechanical strength (Figure 3c). Besides GO, ethylenediamine[41] and epichlorohydrin (ECH)[42] can also lead to the gelation of MXene nanosheets. For instance, ECH used as a cross-linking agent to build covalent bonds between MXene nanosheets and cellulose, due to etherification reactions and hydrogen bond interactions, a $Ti_3C_2T_x$ MXene/cellulose hydrogel with 3D porous structure formed.[42] In another study, hydrothermal treatment of $Ti_3C_2T_x$ MXene in a mixture of thiourea dioxide and ammonia solution resulted in a 3D N-doped $Ti_3C_2T_x$ aerogel as well, with an enlarged BET specific surface area of 108 m^2 g^{-1}.[43]

Liquid–liquid interface self-assembly method can also be used to build 3D MXenes (Figure 3d).[44] For instance, hydrophilic $Ti_3C_2T_x$ dispersed in water and oil-soluble amine-functionalized polyhedral oligomeric silsesquioxane dissolved in toluene interacted at the oil–water interface. A significant reduction in the interfacial tension of the water-toluene system, resulted in a layer of overlapping MXene nanosheets.[44a] After vigorously homogenizing the mixture, stable water-in-oil Pickering emulsions at a water/oil ratio of 1:8 were obtained. Unlike conventional Pickering emulsions with spherical shapes, all the droplets exhibited highly irregular configuration because of the very rapid interfacial jamming of the MXene-based nanoparticles. A lightweight, hydrophobic and isotropic 3D MXene aerogel with excellent mechanical properties was easily prepared by freeze-drying the concentrated emulsion droplets, where the pore size and shape were commensurate with those of the emulsion droplets (Figure 3e,f).[44a] A high concentrated
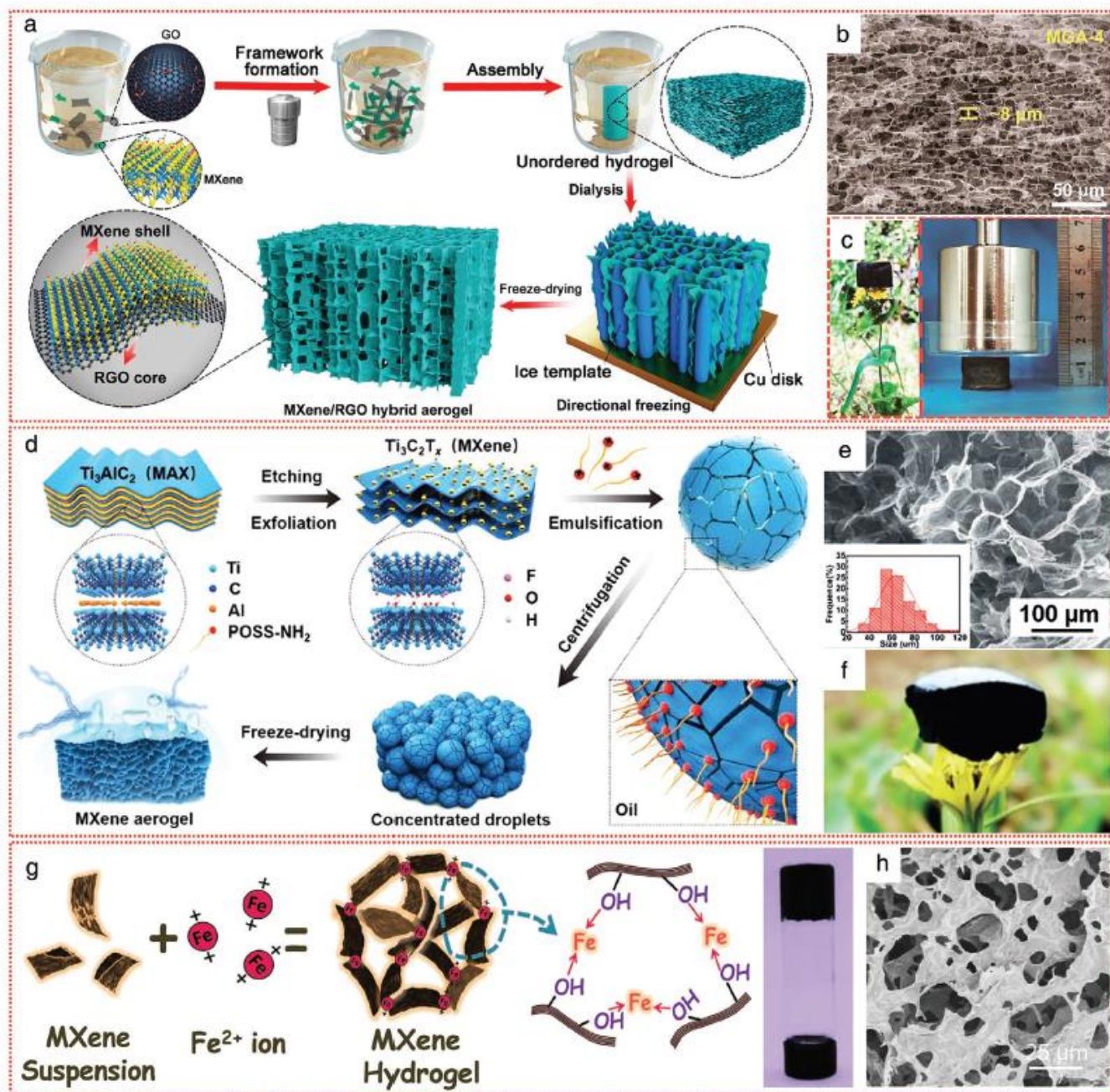
Figure 3. Assembly methods for manufacturing 3D MXene architectures. a) Schematic illustrating the fabrication process of a 3D $Ti_3C_2T_x$ MXene/rGO hybrid aerogel. b) Side-view SEM image of 3D MXene/rGO aerogel. c) Digital images of a 3D MXene/rGO aerogel (100 mg) standing on a flower (left) and supporting a weight of 500 g (right). Reproduced with permission.[40a] Copyright 2018, American Chemical Society. d) Schematic showing the construction of 3D $Ti_3C_2T_x$ MXene aerogels by liquid–liquid interface self-assembly method. e) SEM image of the 3D $Ti_3C_2T_x$ aerogel. f) A small piece of MXene aerogel on a flower. Reproduced with permission.[44a] Copyright 2019, Wiley-VCH. g) Schematic of the metal ion-initiated interaction of MXene nanosheets and photo of the MXene hydrogel. h) SEM image of the MXene monolith. Reproduced with permission.[39b] Copyright 2019, Wiley-VCH.

cetyltrimethylammonium bromide-doped MXene (>24 mg mL^{-1}) was also stabilized at the interface of dodecane and water, resulting in a semisolid and foam-like microstructure, and finally a 3D MXene foam.[44b]

Etched $Ti_3C_2T_x$ MXene nanosheets are negatively charged (zeta potential around −40 mV),[45] therefore, they can be homogeneously dispersed in aqueous solution due to electrostatic

repulsion.[46] By introducing positively charged species in solution, the electrostatic repulsion forces between MXene nanosheets are shielded, leading to the assembly of MXenes into 3D frameworks. In a typical process,[39b] MXene dispersion with a concentration of 10 mg mL^{-1} was added to a $FeCl_2 \cdot 4H_2O$ solution (the mass ratio of $FeCl_2$ to MXene is from 3:8 to 4:1) and a hydrogel was formed in a few minutes (Figure 3g), being

composed by 95 wt% water. The well-shaped hydrogel remained in place even when the tube was inverted, and, after freeze-drying, the MXene monolith showed an interlinked 3D network (Figure 3h). The Fe^{2+}-mediated assembly of MXenes can be divided into two steps. First, electrical interactions between Fe^{2+} and functional groups on MXene surface hinder the electrostatic repulsive force between MXene nanosheets, due to the negative surface charge of MXenes in water. Afterwards, the assembly of MXene nanosheets is assisted by the Fe^{2+} ions as linking agents, resulting in a 3D MXene hydrogel. Interestingly, the 3D MXene hydrogels can also be fabricated with assistance of other multivalent ions, such as divalent (Mg^{2+}, Co^{2+}, Ni^{2+}) and trivalent (Al^{3+}) ions, while univalent ions, such as K^+, H^+,[47] Li^+, Na^+, K^+, TBA^+,[48] and NH_4^+[39c] only lead to the coagulation of MXenes. Most likely, due to the low hydration energy of univalent cations, the bonds established with $-OH$ groups on the surface of MXenes is too poor for gelation, even at high $Ti_3C_2T_x$ concentration (15 mg mL^{-1}) and high Na^+ ions concentration (24 M).[48] Despite initiating the gelation of MXene, some trivalent ions with high oxidation ability, such as Fe^{3+} and Co^{3+}, can as well oxidize MXenes.[39b]

2.3. 3D Printing Method

Additive manufacturing technology, also known as 3D printing, is an emerging technology that allows scalable manufacture of various 3D objects and complex structures, from suitable inks.[49] As MXene inks can feature favorable viscosity and shear-thinning rheological behavior,[22b,50] it is expected to bring 2D MXene nanosheets into 3D architectures by printing.

For example, $Ti_3C_2T_x$ inks with concentrations above 50 mg mL^{-1} can easily flow through narrow nozzles and instantaneously recover their solid-like behavior, retaining the nozzle's filamentary shape after extrusion, resulting in a programmed 3D MXene structure (**Figure 4**a).[51] Morphological characterization showed that the individually printed filaments (mean diameter of about 326 µm) formed a stable 3D structure without overlapping or internal collapse. At a structural level, the $Ti_3C_2T_x$ nanosheets were organized into an internal network with pore size ranging from 3 to 35 µm. The specific surface area of the 3D printed $Ti_3C_2T_x$ architectures was calculated as 177 m^2 g^{-1}, which is considerably higher than previous reports (normally below 80 m^2 g^{-1}).[52]

2.4. Other Preparation Methods

Electrospinning is a simple, versatile, and cost-effective method for manufacturing 3D polymer networks with tunable fiber diameter and porosity.[53] In a typical process, an electrical potential is applied between a droplet of a polymer solution/melt and a grounded target. When the applied electric field overcomes the surface tension of the droplet, a charged jet of polymer solution is ejected and grows longer and thinner until it solidifies or is collected on the target.[54] These fibers stack randomly on each other and form 3D networks. Polyethylene oxide (PEO), polyacrylic acid (PAA), polyvinyl alcohol (PVA),

polyurethane (PU), polyacrylonitrile (PAN), and polycaprolactone (PCL) are the most commonly employed polymers for electrospinning.[55] They can be easily mixed with $Ti_3C_2T_x$ MXene in aqueous or polar organic solvents.[56] For example, $Ti_3C_2T_x$ mixed with PVA in water resulted in a homogenous mixture. After electrospinning under an applied voltage of 18 kV, a $Ti_3C_2T_x$/PVA composite network with abundant mesopores was obtained (Figure 4b).[57] Following the same approach, a $Ti_3C_2T_x$/PAN composite network was successfully produced in N,N-dimethylformamide as well. In this case, the $Ti_3C_2T_x$ MXene nanosheets were found inside of the polymer fibers. Moreover, this $Ti_3C_2T_x$/PAN composite could be easily converted into a 3D $Ti_3C_2T_x$/carbon network via carbonization without structure breakage.[58] Other examples of MXene-based 3D networks prepared by electrospinning include $Ti_3C_2T_x$/PEO,[59] $Ti_3C_2T_x$/chitosan,[60] $Ti_3C_2T_x$/PAA,[61] $Ti_3C_2T_x$/alginate/PEO,[61] $Ti_3C_2T_x$/PVA/PAA/Fe_3O_4,[62] among others.

Gas foaming technology is also commonly used for preparing 3D architectures.[63] As an example, hydrazine reacted with $-OH$ groups on $Ti_3C_2T_x$ MXene surface at 90 °C, generating O_2, CO, and CO_2. The large amounts of gaseous species assured a fast establishment of high pressure between MXene nanosheets, which countered the van der Waals forces that hold the nanosheets together. Consequently, numerous small pores formed between the parallel layers, along with a thickness increment, resulting in a well-defined 3D porous MXene foam (Figure 4c).[64] Notably, because of the removal of hydrophilic groups, this MXene foam exhibited a hydrophobic character.

3. 3D MXene Architectures for Energy Storage Applications

Supercapacitors and rechargeable batteries are becoming more and more important in our daily life because of their high power and energy densities for powering portable electronics and vehicles. 3D MXene architectures with open structures, abundant surface groups, high electrical conductivity and high ion/electron transfer efficiency, hold great potential for designing high-performance supercapacitors and rechargeable batteries.

3.1. Supercapacitors

Electrochemical capacitors, also called supercapacitors, store energy using either ion adsorption (electrochemical double-layer capacitors) or fast surface redox/intercalation reactions (redox-capacitors). They can complement or replace batteries in electrical energy storage and harvesting applications, when high power delivery or uptake is needed.[65] The traditional electrode materials for supercapacitors are carbons,[66] conducting polymers,[67] and transition metal oxides/sulfides.[68] However, they mostly suffer from low practical capacitance, limited electrical conductivity or short cycle life,[15a,69] which may not necessarily meet the ever-increasing demands for modern electronics.

The unique structure of MXenes renders them particularly attractive for energy storage applications because: 1) a conductive inner transition metal carbide layer enables fast electron
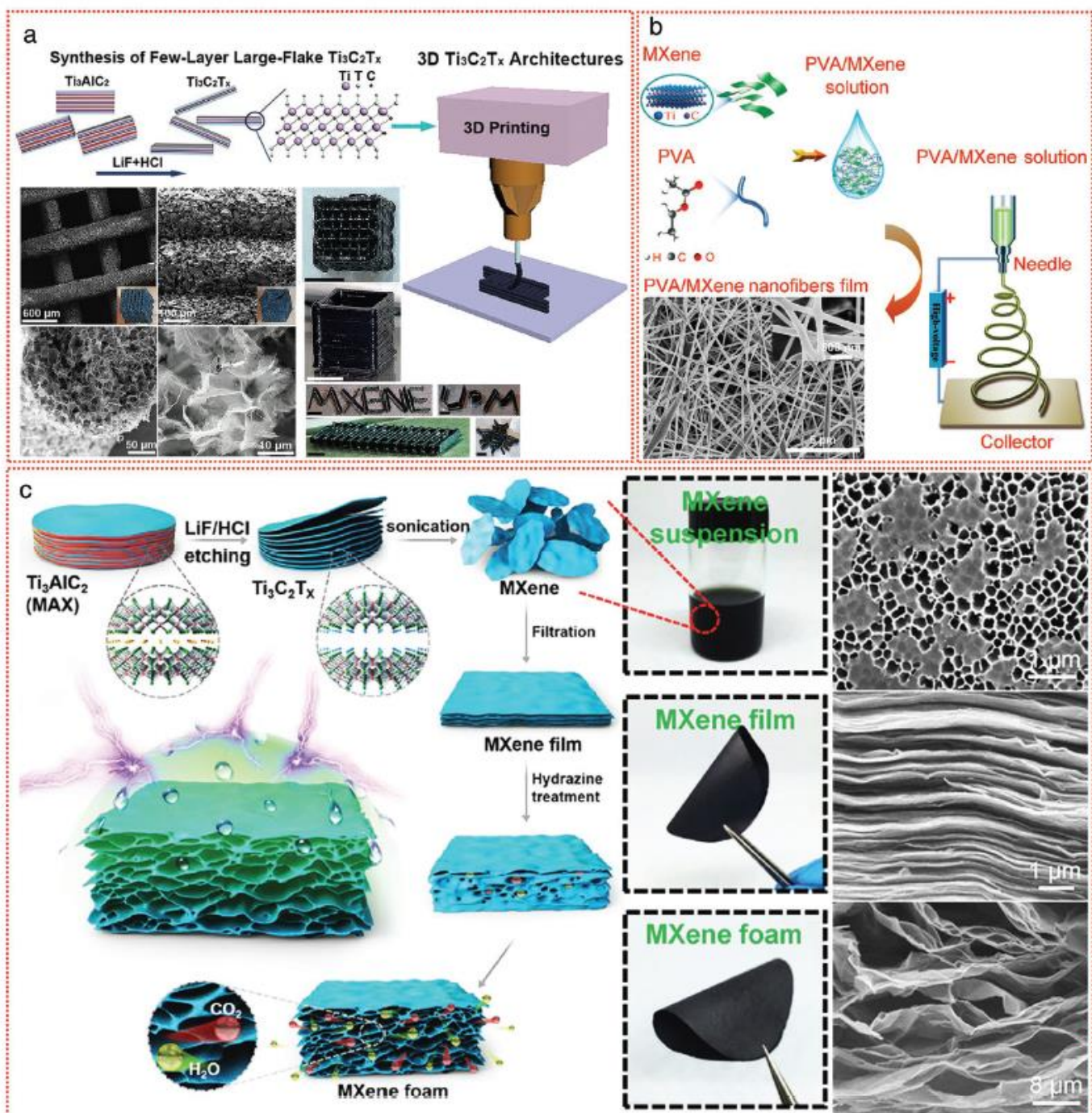
Figure 4. Other methods for manufacturing 3D MXene architectures. a) Schematic representation of the 3D printing method for preparing 3D MXenes. Inset shows the digital photos and SEM images of 3D MXene. Reproduced with permission.[51] Copyright 2019, Wiley-VCH. b) Electrospinning method for preparing 3D PVA/MXene, inset shows the SEM image of PVA/MXene. Reproduced with permission.[57] Copyright 2019, Elsevier Ltd. c) Schematic illustration of the gas foaming technology for preparing 3D porous MXene (left). Photos and SEM images of the MXene suspension, MXene film and MXene foam are shown in right. Reproduced with permission.[64] Copyright 2017, Wiley-VCH.

supply to electrochemically active sites; 2) a transition metal oxide-like surface is redox-active and 3) a 2D morphology and preintercalated water enable fast ion transport (**Figure 5**a).[11] A variety of cations can be intercalated into MXene sheets, offering high volumetric electrochemical performance. For example, the $Ti_3C_2T_x$ MXene film demonstrated a competitive pseudocapacitance of 350 F cm^{-3} by K$^+$ cation intercalation.[10b]

By integrating carbon nanotube (CNT) or PVA in between MXene nanosheets, the capacitance of MXene films can be further enhanced, specifically, 390 F cm^{-3} for CNT/$Ti_3C_2T_x$ in $MgSO_4$ electrolyte[70] and 528 F cm^{-3} for PVA/$Ti_3C_2T_x$ in KOH electrolyte.[71] In H_2SO_4 electrolyte, super high volumetric capacitances of up to 900[72] and 1500 F cm^{-3}[11] were obtained for $Ti_3C_2T_x$ films and $Ti_3C_2T_x$ hydrogels, respectively. Besides
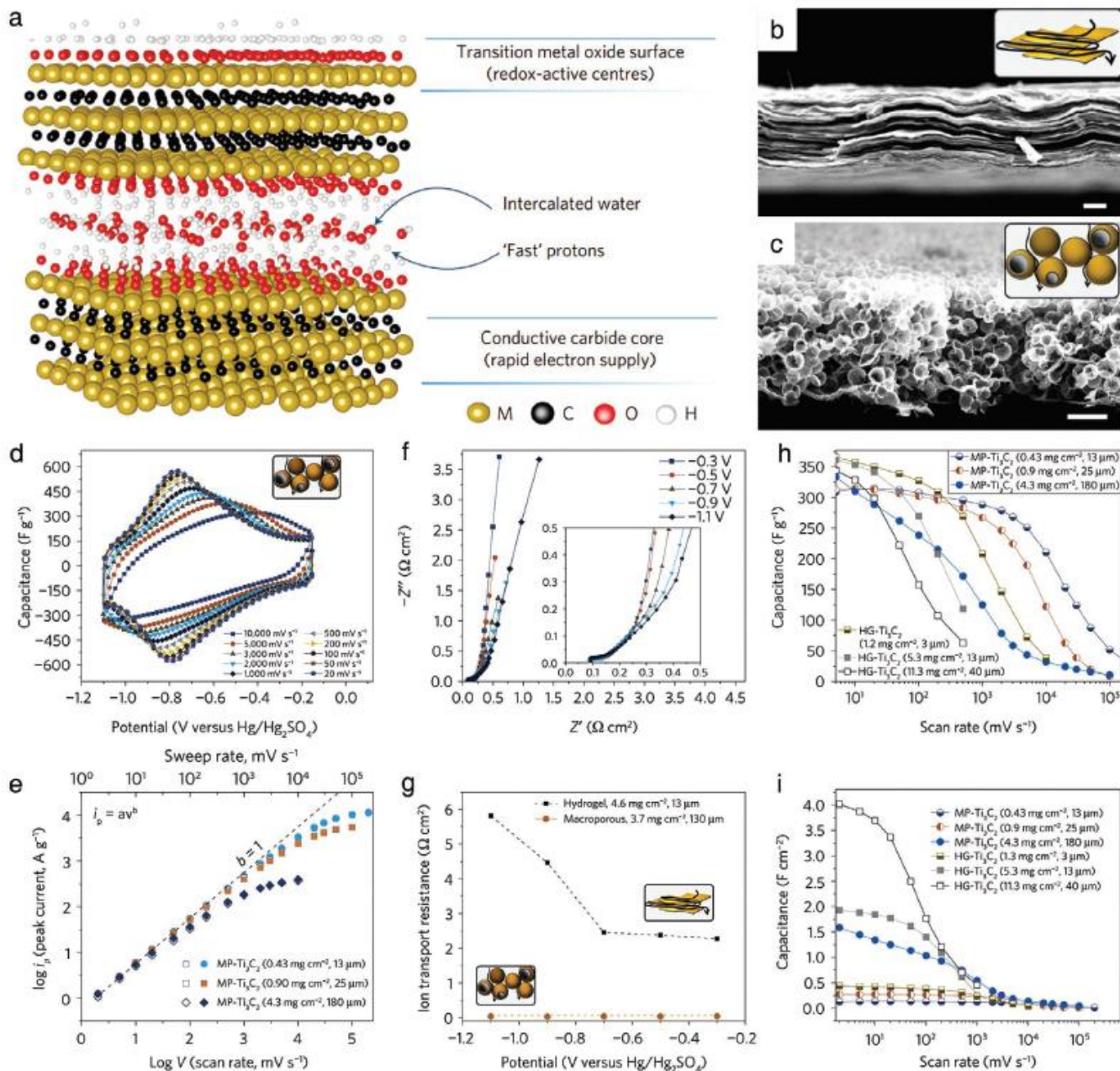
Figure 5. 3D MXene architectures for supercapacitors. a) Schematic of MXene-facilitated proton exchange with water intercalation for energy storage. b) SEM image of $Ti_3C_2T_x$ MXene hydrogel. c) SEM image of macroporous templated $Ti_3C_2T_x$ electrode. Scale bars, 5 µm. Insets in b) and c) show schematically the ionic current pathway in electrodes of different architectures. d) Cyclic voltammetry profiles of a macroporous 13 µm thick film collected in 3 M H_2SO_4. The inset shows schematically macroporous electrode architecture and ionic current pathways in it. e) Determination of the slope, b, for the logarithm of anodic (open symbols) and cathodic (filled symbols) peak current versus logarithm of scan rate for macroporous films with different mass loadings. f) Electrochemical impedance spectroscopy data collected at different potentials for a macroporous film. g) Comparison of ion transport resistance for hydrogel and macroporous electrodes extracted from electrochemical impedance spectroscopy collected at different applied potentials. The insets show schematically the ionic current pathway in hydrogel (top) and macroporous (bottom) electrodes. h,i) Rate performance of MXene films with different preparation methods and mass loadings represented in gravimetric h) and areal i) capacitance. Reproduced with permission.[11] Copyright 2017, Nature Publishing Group.

$Ti_3C_2T_x$, other MXenes, such as the Mo_2CT_x film, also delivered a high volumetric capacitance of 700 F cm^{-3}.[73] However, for the majority of reported MXene electrodes, their rate capabilities are moderate when the electrode thickness exceeds a couple of microns, because of the long ion transport pathways caused by the highly aligned stacked MXene nanosheets (Figure 5b).

Integrating 2D materials into 3D porous framework has proved to be an effective method offering a more open structure with larger specific surface area, which is beneficial for facilitating ionic and electronic transport in electrode materials and thus improving their electrochemical performance.[74] For instance, by using PMMA spheres as templates, a 3D
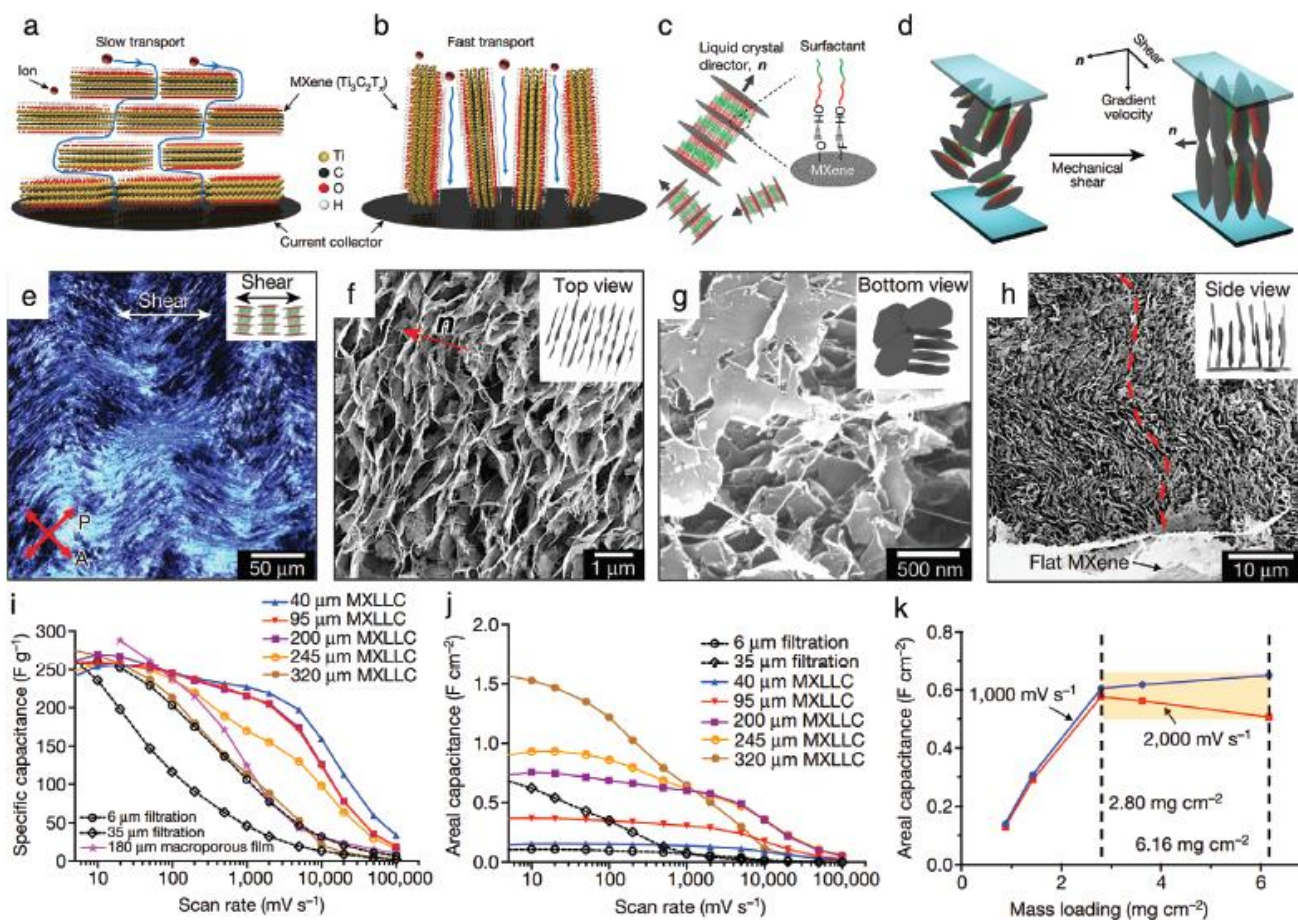
Figure 6. 3D MXene architectures for supercapacitors. Ion transport in a) horizontally stacked and b) vertically aligned $Ti_3C_2T_x$ MXene films. c) Illustration of the surfactant enhanced lamellar structure of the MXLLC. d) Illustration of the alignment method. e) Polarized optical microscope image of the light retardation plate of the MXLLC. f) Top view of SEM image of the MXLLC. Bottom g) and side h) views of vertical nanosheets on the horizontally aligned MXene current collector. i) Rate performance of vacuum-filtered MXene papers, MXLLC films and a 180 μm thick macroporous MXene film at scan rates ranging from 10 to 100 000 mV s^{-1}. j) Areal capacitance of vacuum-filtered MXene papers and MXLLC films at scan rates ranging from 10 to 100 000 mV s^{-1}. k) Areal capacitance as a function of the mass loading of the MXLLC films at scan rates of 1000 and 2000 mV s^{-1}. Reproduced with permission.[77] Copyright 2018, Nature Publishing Group.

macroporous $Ti_3C_2T_x$ (MP-$Ti_3C_2T_x$) MXene (Figure 5c) was prepared.[11] Compared to the rapid decrease of gravimetric and volumetric capacitance of the $Ti_3C_2T_x$ hydrogel (HG-$Ti_3C_2T_x$) at scan rates above 500 mV s^{-1}, the MP-$Ti_3C_2T_x$ electrodes revealed a more exceptional rate handling ability (Figure 5d,e,h,i), with gravimetric capacitance of 310 F g^{-1} at 10 mV s^{-1} (0.135 F cm^{-2}) and 210 F g^{-1} (0.090 F cm^{-2}) at 10 V s^{-1} for a 13 μm thick film, surpassing some of the best-reported results.[75] Moreover, a 180 μm thick macroporous film demonstrated a capacitance of 125 F g^{-1} (0.54 F cm^{-2}) at 1 V s^{-1} (Figure 5h). The superior rate capability of the macroporous electrode was further proved by the ultralow ion transport resistance of 0.04 Ω cm^2 across all potentials (Figure 5f,g). Even in organic electrolyte with low ionic conductivity, the 3D macroporous $Ti_3C_2T_x$ electrodes still delivered a high capacitance of 195 F g^{-1} (410 F cm^{-3}) at 2 mV s^{-1} and exhibited a high capacitance retention of 61% at 1000 mV s^{-1}, over a wide voltage window of 2.4 V.[21d] This successful 3D macroporous electrode strategy also suits for other MXenes, such as the Mo_2CT_x, the porous Mo_2CT_x electrode

with a thickness of 30 μm yielded a capacitance of ≈130 F g^{-1} at an ultrahigh scan rate of 1 V s^{-1} in H_2SO_4 electrolyte.[11]

Vertical alignment of 2D materials facilitates fast ion transport, shortens ion diffusion paths, and favors ion access to electrodes, resulting in thickness-independent electrochemical performances in thick films.[76] The vertically aligned $Ti_3C_2T_x$ MXene lamellar liquid crystal (MXLLC) films (**Figure 6a–h**) showed two pairs of redox peaks, and which remained mostly independent of film thickness from 40 up to 200 μm, prominently surpassing the horizontally stacked filtrated films. Besides, the characteristic parameter b kept nearly 1 between 5 and 2000 mV s^{-1} for films up to 200 μm thick, reflecting ultrafast surface reactions-controlled charge-storage kinetics of the MXLLC films with thickness-independent behavior. In addition, the 200 μm thick MXLLC film demonstrated excellent retention with a capacitance of over 200 F g^{-1} (areal capacitance greater than 0.6 F cm^{-2}) at a high scan rate of 2000 mV s^{-1}, which is better than filtrated and macroporous films (Figure 6i,j). Moreover, the areal capacitance at scan rates of 1000–2000 mV s^{-1}

Table 1. Comparison of 3D MXene architectures for supercapacitor applications.

3D MXene architectures	Electrolyte	Capacitance at low rate	Capacitance at high rate	Cycling stability	Refs.
Porous $Ti_3C_2T_x$ film	3 M H_2SO_4	310 F g^{-1} (10 mV s^{-1})	210 F g^{-1} (10 V s^{-1})	95% (10 000)	[11]
Porous Mo_2CT_x film	3 M H_2SO_4	≈160 F g^{-1} (10 mV s^{-1})	≈130 F g^{-1} (1 V s^{-1})	NA	[11]
Porous $Ti_3C_2T_x$ film	1 M LiTFSI in propylene carbonate	195 F g^{-1} (2 mV s^{-1})	120 F g^{-1} (1000 mV s^{-1})	94% (10 000)	[21d]
Porous $Ti_3C_2T_x$ film	3 M H_2SO_4	≈250 F g^{-1} (10 mV s^{-1})	≈155 F g^{-1} (10 V s^{-1})	100% (20 000)	[77]
$Ti_3C_2T_x$ hydrogel	3 M H_2SO_4	271 F g^{-1} (2 mV s^{-1})	226 F g^{-1} (1V s^{-1})	97.1% (10 000)	[39b]
$Ti_3C_2T_x$ aerogel	3 M H_2SO_4	404 F g^{-1} (0.5 A g^{-1})	283 F g^{-1} (20 A g^{-1})	96% (8000)	[30f]
$Ti_3C_2T_x$ aerogel	3 M H_2SO_4	438 F g^{-1} (10 mV s^{-1})	349 F g^{-1} (2 V s^{-1})	90% (20 000)	[43]
$Ti_3C_2T_x$ foam	1 M KOH	271.2 mF cm^{-2} (5 mV s^{-1})	177.7 mF cm^{-2} (100 mV s^{-1})	88.7% (10 000)	[80]
$Ti_3C_2T_x$/rGO aerogel	2 M $ZnSO_4$	123.2 F g^{-1} (2 mV s^{-1})	38.5 F g^{-1} (100 mV s^{-1})	95% (75 000)	[28]
$Ti_3C_2T_x$/rGO hydrogel	NA	370 F g^{-1} (5 A g^{-1})	165 F g^{-1} (1000 A g^{-1})	98% (10 000)	[41b]
Carambola-like $Ti_3C_2T_x$/polypyrrole	1 M H_2SO_4	416 F g^{-1} (0.5 A g^{-1})	208 F g^{-1} (8 A g^{-1})	86.4% (5000)	[78]
$Ti_3C_2T_x$/NiO aerogel	1 M Na_2SO_4	341 F cm^{-3} (2 mV s^{-1})	≈110 F cm^{-3} (100 mV s^{-1})	114% (2500)	[37]
Porous $Ti_3C_2T_x$/bacterial cellulose film	3 M H_2SO_4	416 F g^{-1} (3 mA cm^{-2})	260 F g^{-1} (50 mA cm^{-2})	96.5% (10 000)	[79]
$Ti_3C_2T_x$/nickel–aluminum layered double hydroxide network	6 M KOH	665 F g^{-1} (1 A g^{-1})	333 F g^{-1} (10 A g^{-1})	70% (4000)	[81]
Co_3O_4/$Ti_3C_2T_x$/rGO aerogel	6 M KOH	345 F g^{-1} (1 A g^{-1})	NA	85% (10 000)	[36]
$Ti_3C_2T_x$/rGO aerogel	PVA/H_2SO_4	34.6 mF cm^{-2} (1 mV s^{-1}) (device)	9.2 mF cm^{-2} (100 mV s^{-1}) (device)	91% (15 000)	[31b]
AC/CNT/$Ti_3C_2T_x$/rGO network	PVA/H_2SO_4	70.1 mF cm^{-2} (10 mV s^{-1}) (device)	62.5 mF cm^{-2} (100 mV s^{-1}) (device)	92% (7000)	[22a]
$Ti_3C_2T_x$ network	PVA/H_2SO_4	242.5 F g^{-1} (0.2 A g^{-1}) (device)	117.7 F g^{-1} (5 A g^{-1}) (device)	90% (10 000)	[51]

is about the same for mass loadings in the range of 2.80 to 6.16 mg cm^{-2} (Figure 6k), showing the possibility of using vertically aligned MXenes to enable thick electrodes operating at very high charge–discharge rates.[77]

Besides pure 3D MXenes, 3D MXene-based composites with different components and features, such as MXene/graphene,[28,31b,41b] MXene/PANI,[15a] MXene/polypyrrole,[78] MXene/cellulose,[79] MXene/NiO,[37] and MXene/rGO/Co_3O_4,[36] also exhibited impressive electrochemical performance. For example, the 3D porous $Ti_3C_2T_x$/cellulose composite delivered a high specific capacitance of 416 F g^{-1} at 3 mA cm^{-2} and a high capacitance retention with 260 F g^{-1} at 50 mA cm^{-2}, which was much higher than that of the pure $Ti_3C_2T_x$ MXene electrodes (318 F g^{-1} at 3 mA cm^{-2} and 87 F g^{-1} at 50 mA cm^{-2}).[79] Clearly, the 3D nature of the formed structures provides great advantages, such as: 1) 3D porous network allows for vast ion storage and rapid ion transport; 2) short ion transport length favors more efficient ion diffusion; 3) large ion-accessible active surface; and 4) high electrical conductivity from interconnected MXene nanosheets. Moreover, even after mechanically compressing the 3D $Ti_3C_2T_x$/PANI composite, the electrode still showed high specific capacitances of 510 F g^{-1} at 10 mV s^{-1} and 407 F g^{-1} at 1000 mV s^{-1} in a 3 M H_2SO_4 electrolyte. A higher specific capacitance of 579 F g^{-1} at 10 mV s^{-1} could be achieved with higher PANI content. It is worth noting that this is the first reported high-performance MXene-based positive electrode, as proved by both experiments and first-principle calculations.[15a] The electrochemical performances of 3D MXene architectures for supercapacitors are summarized in **Table 1**.

3.2. Lithium-Ion Batteries

Owing to the non-memory effect and enhanced energy densities, rechargeable lithium-ion batteries (LIBs) have attracted intense interest and have been widely used in portable electronics and electrical vehicles for the past few decades.[82] As the most important component of LIBs, electrode materials play a key role in determining their performance. 2D materials, especially the emerging MXenes, show great potential for the next generation LIBs electrodes because of their high theoretical capacity, high electric conductivity, and wide chemical and structural variety.[9d,83]

MXenes can accommodate lithium ions in between the layers by forming $M_{n+1}X_nT_xLi_y$, for example, $Ti_3C_2O_2Li_2$.[84] In addition, owing to the 2D nature and conductivity of MXenes, an additional layer of lithium ions can be reversibly formed, providing a twofold boost of the electrode capacity (**Figure 7a**).[84a,85] Lots of factors are found to significantly affect the lithium storage performance of MXenes, such as surface functional groups, formula weights, and transition metal species. Oxygen terminations can lead to the highest capacity, whereas hydroxyls and fluorines result in lower capacities as well as lithium-ion transport deterioration.[84b,86] MXenes with low formula weights, such as M_2X (Ti_2C, Nb_2C, V_2C, Sc_2C, among others) electrodes, usually show higher gravimetric capacities than their M_3X_2 and M_4X_3 counterpart.[87] However, there are some exceptions. Niobium atoms are heavier than titanium ones, but Nb_2CT_x still shows higher gravimetric capacity than Ti_2CT_x at the same cycling rate (180 mAh g^{-1} for Nb_2CT_x versus 110 mAh g^{-1} of Ti_2CT_x at 1 C).[88]
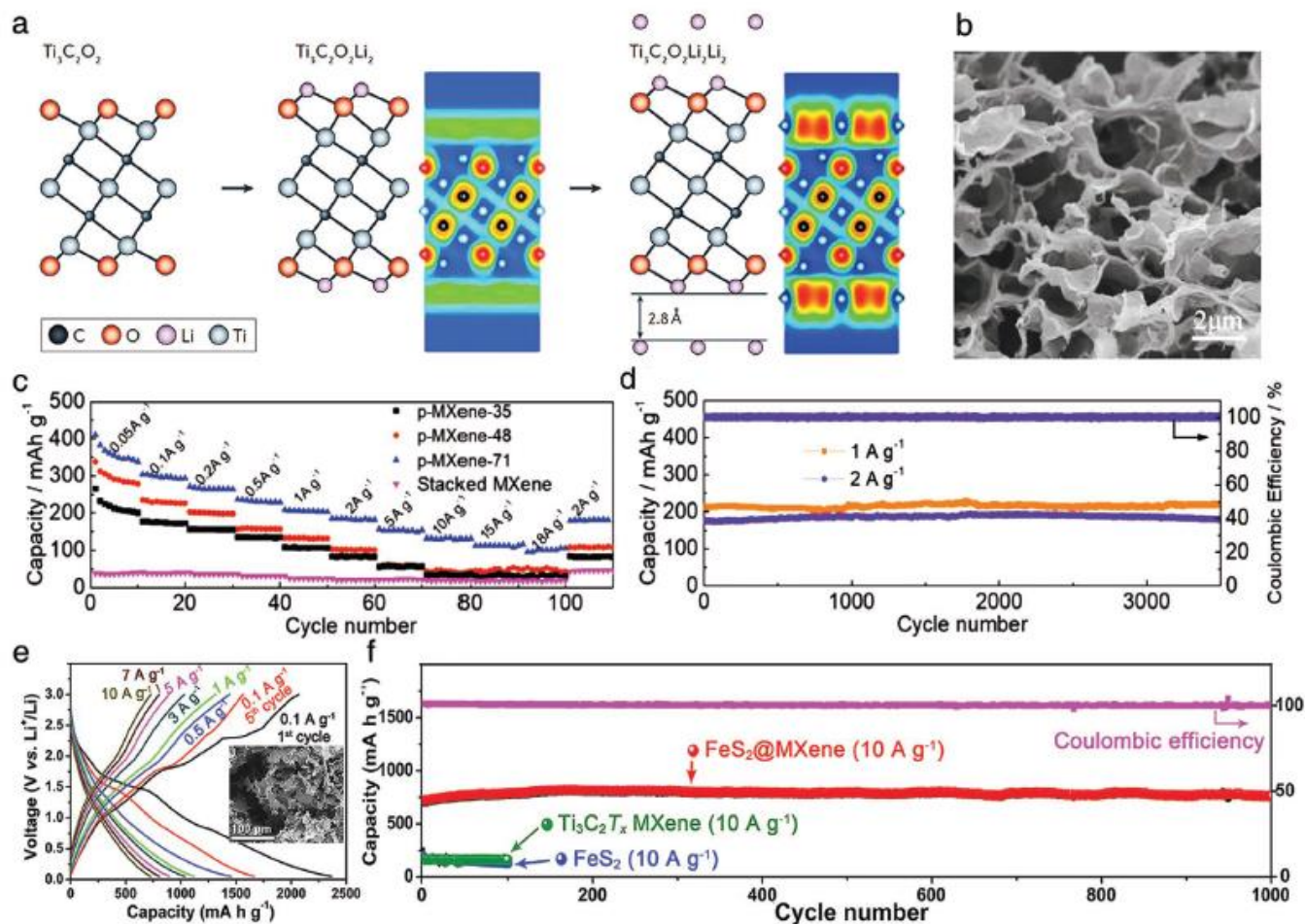
Figure 7. 3D MXene architectures for LIBs. a) Schematic illustration of the $Ti_3C_2T_x$ lithiation process. The valence electron localization functions are shown with and without the additional lithium layer. Reproduced with permission.[91] Copyright 2017, Nature Publishing Group. b) SEM image of the 3D porous $Ti_3C_2T_x$ MXene foam. c) Rate performance of the stacked MXene film and the 3D porous MXene foams. d) Long-term cycle stability of the 3D porous $Ti_3C_2T_x$ MXene electrode. Reproduced with permission.[23b] Copyright 2019, Wiley-VCH. e) Charge–discharge profiles of 3D FeS₂@MXene for lithium ion storage, inset is the SEM image of 3D FeS₂@MXene. f) Long-time galvanostatic cycling performance of 3D FeS₂@MXene nanohybrid, pure FeS₂, and $Ti_3C_2T_x$ MXene for Li-ion storage at the current densities of 10 A g⁻¹, respectively. Reproduced with permission.[89] Copyright 2018, American Chemical Society.

Besides inherent material properties, electrode structure is another important determinant of electrochemical performance of MXene materials.[9f] In striking contrast to 2D stacking structure, 3D porous electrode architectures can effectively facilitate ions transport and improve the utilization of MXene nanosheets, resulting in improved lithium storage performance (**Table 2**). For example, a stacked $Ti_3C_2T_x$ MXene film exhibited a relatively low specific surface area of 1.9 m² g⁻¹ and a low capacity of 35.4 mAh g⁻¹. In contrast, a sulfur-template 3D $Ti_3C_2T_x$ foam (Figure 7b) with open structure and an enlarged specific surface area of 39.9 m² g⁻¹ exhibited a significantly enhanced capacity of 455.5 mAh g⁻¹ at 50 mA g⁻¹, an excellent rate performance (101 mAh g⁻¹ at 18 A g⁻¹) and a superior ultralong-term cycle stability (220 mAh g⁻¹ at 1 A g⁻¹ after 3500 cycles) (Figure 7c,d),[23b] demonstrating the great advantages of porous electrode architectures for lithium storage. By combining the MXene with rGO, a 3D porous $Ti_3C_2T_x$/rGO composite film with less stacking of MXene nanosheets was also obtained. This hybrid inherited the advantage of graphene in

the formation of a porous structure and of MXene by showing high electrical conductivity, leading to a weaker stacking of MXene nanosheets and a facilitated electrolyte ions infiltration efficiency in electrodes. The resultant 3D porous $Ti_3C_2T_x$/rGO film showed a high specific capacity of 335.5 mAh g⁻¹ at 0.05 A g⁻¹, a good rate capability with 30% capacitance retention at 4 A g⁻¹, and no capacity decay after 1000 cycles.[39c]

To further improve the Li-ion storage ability of 3D MXenes, various transition metal oxides or sulfides were introduced. The resulting 3D MXene-based nanocomposites combined both high conductivity, high porosity of 3D MXene framework and high specific capacity of redox materials, favoring a remarkably enhanced electrochemical performance. For example, the 3D FeS₂@$Ti_3C_2T_x$ nanohybrid with ≈10 nm FeS₂ nanodots homogeneously anchored on the surface of 3D MXene presented high specific capacities of 1728 mAh g⁻¹ at 0.1 A g⁻¹ and 601 mAh g⁻¹ at 10 A g⁻¹ for Li-ion storage, respectively (Figure 7e). Its long-term stability was also remarkable. After 1000 cycles at a current density of 10 A g⁻¹, the 3D FeS₂@$Ti_3C_2T_x$ nanohybrid

Table 2. Comparison of 3D MXene architectures for rechargeable battery applications.

3D MXene architectures	Types	Current density	Cycle number	Capacity retention	Refs.
Porous $Ti_3C_2T_x$ film	LIBs	0.05 A g^{-1}	300	314.9 mAh g^{-1}	[23b]
		1 A g^{-1}	3500	220 mAh g^{-1}	
Porous $Ti_3C_2T_x$/rGO film	LIBs	1 A g^{-1}	1000	212.5 mAh g^{-1}	[39c]
$Ti_3C_2T_x$/FeS$_2$ framework	LIBs	10 A g^{-1}	1000	762 mAh g^{-1}	[89]
$Ti_3C_2T_x$/SnO$_2$@C aerogel	LIBs	0.5 A g^{-1}	100	509 mAh g^{-1}	[91]
		1 A g^{-1}	1000	520 mAh g^{-1}	
		2 A g^{-1}	1000	492 mAh g^{-1}	
		5 A g^{-1}	1000	301.6 mAh g^{-1}	
		10 A g^{-1}	1000	169 mAh g^{-1}	
Hollow $Ti_3C_2T_x$/CoO/Co$_2$Mo$_3$O$_8$ network	LIBs	0.1 A g^{-1}	100	936.2 mAh g^{-1}	[92]
		2 A g^{-1}	1200	545 mAh g^{-1}	
$Ti_3C_2T_x$/Na$_{0.23}$TiO$_2$ network	LIBs	5 A g^{-1}	4000	178 mAh g^{-1}	[107]
$Ti_3C_2T_x$/Na$_{0.23}$TiO$_2$ network	SIBs	2 A g^{-1}	4000	56 mAh g^{-1}	[107]
Porous $Ti_3C_2T_x$ film	SIBs	2.5 C	1000	295 mAh g^{-1}	[21a]
Porous V$_2$CT$_x$ film	SIBs	2.5 C	1000	310 mAh g^{-1}	
Porous Mo$_2$CT$_x$ film	SIBs	2.5 C	1000	290 mAh g^{-1}	
$Ti_3C_2T_x$ network	SIBs	0.1 A g^{-1}	100	180 mAh g^{-1}	[23a]
		1 A g^{-1}	1000	189 mAh g^{-1}	
$Ti_3C_2T_x$ network	SIBs	0.02 A g^{-1}	50	246 mAh g^{-1}	[47]
$Ti_3C_2T_x$ network	SIBs	0.1 A g^{-1}	300	160 mAh g^{-1}	[48]
$Ti_3C_2T_x$ nanoribbons	SIBs	0.05 A g^{-1}	200	113 mAh g^{-1}	[102]
		0.2 A g^{-1}	500	53 mAh g^{-1}	
$Ti_3C_2T_x$/TiO$_2$/rGO/cellulose aerogel	SIBs	1 A g^{-1}	2000	≈105 mAh g^{-1}	[103]
$Ti_3C_2T_x$/Sb$_2$O$_3$ network	SIBs	0.05 A g^{-1}	50	470 mAh g^{-1}	[104]
		0.1 A g^{-1}	100	472 mAh g^{-1}	
$Ti_3C_2T_x$/FeS$_2$ network	SIBs	0.1 A g^{-1}	100	563 mAh g^{-1}	[89]
		5 A g^{-1}	100	291 mAh g^{-1}	
$Ti_3C_2T_x$/NiCoP network	SIBs	0.1 A g^{-1}	100	374.8 mAh g^{-1}	[105]
		1 A g^{-1}	2000	261.7 mAh g^{-1}	
Flower-like $Ti_3C_2T_x$/VO$_2$	SIBs	0.1 A g^{-1}	200	280.9 mAh g^{-1}	[106]
		1 A g^{-1}	200	≈240 mAh g^{-1}	
$Ti_3C_2T_x$/PDDA–NPCN network	SIBs	0.1 A g^{-1}	300	358.4 mAh g^{-1}	[14a]
		1 A g^{-1}	2000	252.2 mAh g^{-1}	
		2 A g^{-1}	2000	151.2 mAh g^{-1}	
$Ti_3C_2T_x$ nanoribbons	PIBs	0.2 A g^{-1}	500	42 mAh g^{-1}	[102]
Porous $Ti_3C_2T_x$ film	MIBs	1 C	60	≈50 mAh g^{-1}	[21c]
$Ti_3C_2T_x$/CNT network	LSBs	0.5 C	1200	≈450 mAh g^{-1}	[52c]
Ti$_2$CT$_x$/CNT network	LSBs	0.5 C	1200	≈450 mAh g^{-1}	
Ti$_3$CNT$_x$/CNT network	LSBs	0.5 C	1200	≈450 mAh g^{-1}	
$Ti_3C_2T_x$/rGO aerogel	LSBs	0.1 C	30	879 mAh g^{-1}	[40b]
		1 C	500	596 mAh g^{-1}	
N-$Ti_3C_2T_x$ network	LSBs	0.2 C	200	950 mAh g^{-1}	[115]
Ti$_3$CNT$_x$/mesoporous carbon network	LSBs	0.5 C	300	704.6 mAh g^{-1}	[120]
Ti$_3$CNT$_x$/MnO$_2$ aerogel	LSBs	1 C	500	501 mAh g^{-1}	[121]
$Ti_3C_2T_x$ nanoribbons-$Ti_3C_2T_x$/PP	LSBs	0.5 C	50	611 mAh g^{-1}	[110c]

still depicted a reversible specific capacity of 762 mAh g^{-1}, which was much higher than pure FeS$_2$ (128 mAh g^{-1} after 100 cycles) and Ti$_3$C$_2$T$_x$ MXene (161 mAh g^{-1} after 100 cycles) (Figure 7f).[89] The significant enhancement of the electrochemical performance can be ascribed to the large surface area and superior electrical conductivity of the unique 3D FeS$_2$@Ti$_3$C$_2$T$_x$ heterostructure. SnO$_2$ is another attractive electrode material because of its high theoretical capacity (782 mAh g^{-1}), nontoxicity, low cost, facile preparation, and good chemical stability.[90] Attributing to 3D Ti$_3$C$_2$T$_x$ conductive network and protective carbon layer, the as-prepared 3D SnO$_2$@C/Ti$_3$C$_2$T$_x$ aerogel framework delivered a high initial capacity (1314 mAh g^{-1}) and a reversible specific capacity up to 520 mAh g^{-1} after 1000 charge–discharge cycles at 1 A g^{-1}. Even at 10 A g^{-1}, it still achieved a reversible specific capacity of 205.6 mAh g^{-1}, with a discharge capacity of 169 mAh g^{-1} and a Coulombic efficiency of 99.5% after 1000 cycles.[91] 3D CoO/Co$_2$Mo$_3$O$_8$@Ti$_3$C$_2$T$_x$ frameworks prepared by electrostatically assembling of the negatively charged MXene and the positively charged layered double hydroxide, also presented a high reversible capacity of 947.4 mAh g^{-1} at 0.1 A g^{-1}, remarkable rate behavior with 435.8 mAh g^{-1} retained at 5 A g^{-1}, and good stability over 1200 cycles (545 mAh g^{-1} at 2 A g^{-1}).[92]

3.3. Sodium-Ion Batteries

LIBs are being widely used in portable electronic devices and large-scale grids storages, which however could be greatly hampered by limited available lithium resources, rising cost, and safety issues. Sodium-ion batteries (SIBs) are regarded as a promising alternative to LIBs because of their rich abundance, low cost, high energy density approaching to LIBs, and similar redox potential ($E_{Na/Na^+} = -2.71$ V vs SHE, $E_{Li/Li^+} = -3.04$ V vs SHE).[93] Unfortunately, the ionic radius of sodium ion (1.02 Å) is larger than lithium ion (0.76 Å), resulting in a totally different electrochemical behavior of SIBs from LIBs. For example, sodium ions even cannot be intercalated into commercially available graphite anodes due to insufficient interlayer space.[94]

With flexible interlayer space and high conductivity, MXenes can accommodate ions with various sizes, showing great potential for high-performance SIBs applications.[9f,95] In fact, theoretical studies also suggest that sodium ions can be electrochemically intercalated/deintercalated into/out of the Ti$_3$C$_2$T$_x$ lattice (**Figure 8a**). This reversible process occurs via a two-phase transition and solid-solution reaction, with a low diffusion barrier (about 0.41 eV).[96] Ex situ NMR spectra during the initial two cycles further proved that, rather than the solvated sodium ions adsorption, desolvated sodium ions intercalation is the main electrochemical reaction accounting for sodiation of Ti$_3$C$_2$T$_x$ (Figure 8b). The interlayer distance remained unchanged during the whole sodiation/desodiation process due to the pillaring effect of trapped sodium ions and the swelling effect of penetrated solvent molecules between the Ti$_3$C$_2$T$_x$ nanosheets. Overall, these effects resulted in high cycle stability and fast sodium ions diffusion.[97] Moreover, the theoretical capacity of nonterminated Ti$_3$C$_2$ MXene was reported to be 351.8 mAh g^{-1},[98] which is very close to that of the commercial graphite for LIBs (372 mAh g^{-1}).[99] Nevertheless, the stacking of MXene nanosheets leads to limited active surface area and thus weakened electrochemical performance.[100] As mentioned before, designing a 3D porous electrode structure can effectively conquer this issue and favor enhanced sodium-ion storage capability. Taking the PMMA-templated macroporous MXene films as an example, the freestanding, flexible, and highly conductive 3D Ti$_3$C$_2$T$_x$, V$_2$CT$_x$, and Mo$_2$CT$_x$ film electrodes exhibited reversible capacities of 330, 340, and 370 mAh g^{-1} at a charging rate of 0.25 C, respectively. At a high current rate of 25 C, the 3D Ti$_3$C$_2$T$_x$, V$_2$CT$_x$ and Mo$_2$CT$_x$ still retained capacities of 120, 125, and 170 mAh g^{-1}, respectively (Figure 8c). Moreover, all 3D MXene films were stable during the entire 1000 cycles, with a Coulombic efficiency close to 100% (Figure 8d).[21a] These values were significantly better than the values obtained on stacked MXenes,[84a,95,96,101] demonstrating once again the advantages of 3D electrode architecture. Besides, sulfur-templated 3D macroporous Ti$_3$C$_2$T$_x$ MXene film,[23a] acid or alkali-induced 3D Ti$_3$C$_2$T$_x$ foam,[47,48] alkalized 3D Ti$_3$C$_2$T$_x$ nanoribbon[102] and freeze-dried 3D rGO/Ti$_3$C$_2$T$_x$/cellulose aerogel[103] all showed improved SIBs performance over the stacked MXenes, due to their more abundant ion access/electron transport channels and richer exposed active surface area (Table 2).

By introducing other electrochemically active materials, the sodium storage performance of 3D MXenes could be further enhanced. 3D Sb$_2$O$_3$/Ti$_3$C$_2$T$_x$ composite with Sb$_2$O$_3$ nanoparticles (sub-50 nm) uniformly incorporated in 3D Ti$_3$C$_2$T$_x$ networks, presented a good structural stability and superior electrochemical performance in SIBs.[104] This was characterized by a high reversible capacity of 444 mAh g^{-1} at 50 mA g^{-1}, an excellent rate performance with a capacity of 295 mAh g^{-1} at 2 A g^{-1}, and an enhanced cycling performance without capacity decay after 100 cycles at 100 mA g^{-1}. This remarkable performance can be attributed to three factors: 1) Sb$_2$O$_3$ nanoparticles serve as sodium ion reservoir; 2) 3D Ti$_3$C$_2$T$_x$ networks provide highly efficient pathways for transport of electrons and sodium ions; and 3) Ti$_3$C$_2$T$_x$ nanosheets buffer the volume expansion of Sb$_2$O$_3$ during sodiation/desodiation. Benefiting from the 3D conductive network, close contact between electrode and electrolyte, and rich redox reaction sites, the 3D Ti$_3$C$_2$/NiCoP electrode also delivered high specific capacities of 416.9, 364.9, 307.6, 278.1, and 240.1 mAh g^{-1} at 0.1, 0.2, 0.5, 1 and 2 A g^{-1}, respectively, which is much higher than that of the Ti$_3$C$_2$T$_x$ electrode (Figure 8e–g).[105] A similar synergistic effect was observed as well for VO$_2$/Ti$_3$C$_2$T$_x$[106] and Na$_{0.23}$TiO$_2$/Ti$_3$C$_2$T$_x$[107] composites with 3D architecture, which demonstrated remarkably improved sodium-ion storage performance. Moreover, by integrating FeS$_2$ on 3D Ti$_3$C$_2$T$_x$, better electrochemical performances than 3D MXene/oxides composites were obtained, including high specific capacity of 665 mAh g^{-1} at 0.1 A g^{-1}, excellent rate capability with 334 mAh g^{-1} at 2 A g^{-1} and outstanding cycling stability.[89] Nevertheless, the electrochemical performance of 3D MXene architectures in SIBs is inferior to that in LIBs, mainly due to the larger ionic radius of sodium ions caused lower adatom content and more sluggish kinetics, in both MXenes and MXene-based composites.[89,98,108]
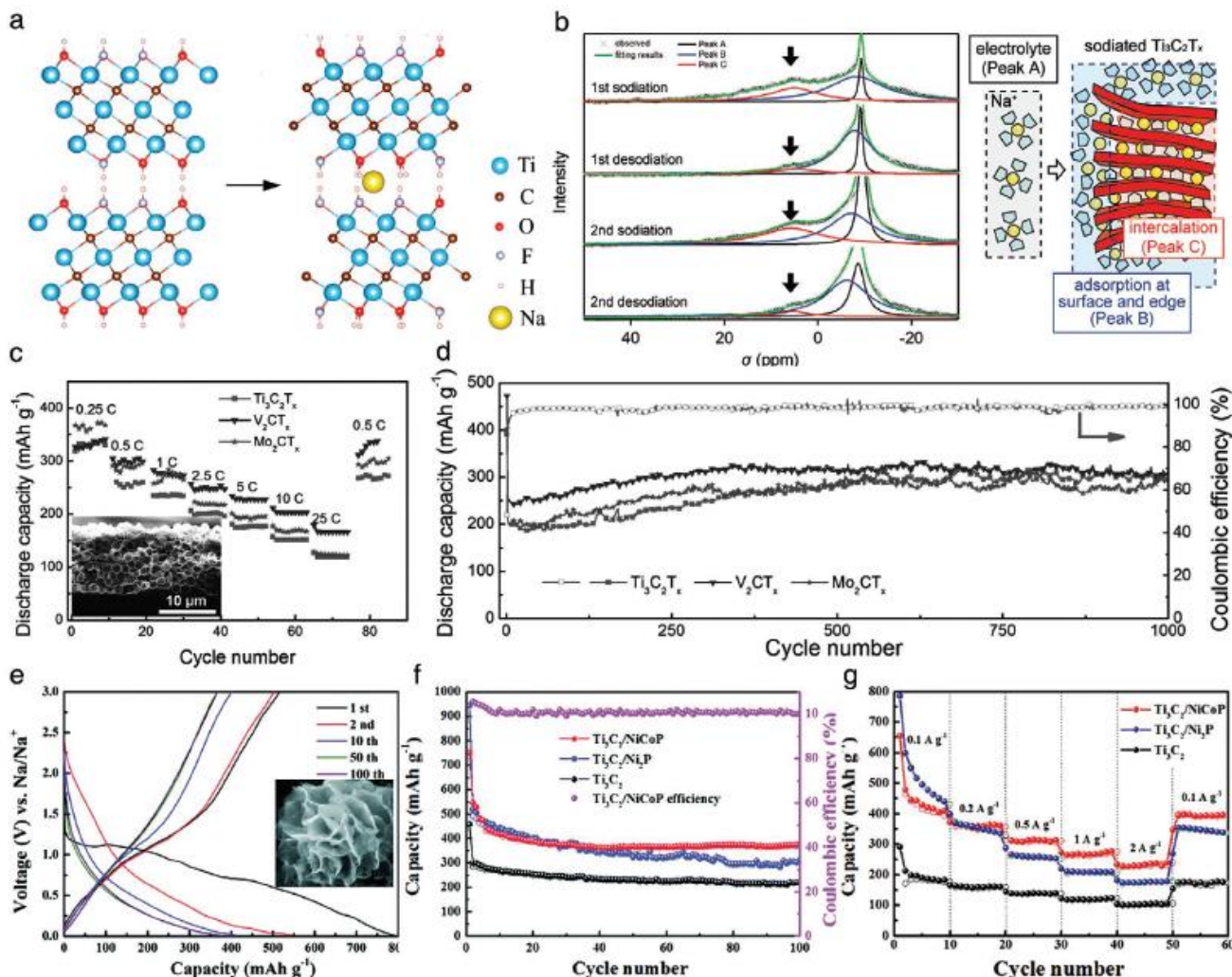
Figure 8. 3D MXene architectures for SIBs. a) Schematic illustration of the $Ti_3C_2T_x$ sodiation process. Reproduced with permission.[96] Copyright 2015, American Chemical Society. b) NMR signals during the initial two cycles can be deconvoluted into three peaks (black, blue, and red lines), which originate from different sodium ion species, as shown in the schematic illustration. Reproduced with permission.[97] Copyright 2016, American Chemical Society. c) Rate profiles of the 3D macroporous MXene film electrodes for sodium-ion storage, inset is the cross-sectional SEM image of the 3D macroporous $Ti_3C_2T_x$ film. d) Long cycling performance of the 3D macroporous MXene film electrodes at 2.5 C. Reproduced with permission.[21a] Copyright 2017, Wiley-VCH. e) Charge-discharge profiles of the 3D $Ti_3C_2/NiCoP$ electrode, inset is the SEM image of the 3D $Ti_3C_2/NiCoP$. f) Cycling performance of the three electrodes. g) Rate capability of the three electrodes. Reproduced with permission.[105] Copyright 2019, The Royal Society of Chemistry.

3.4. Metal-Ion Batteries Beyond Lithium and Sodium

In addition to lithium ions and sodium ions, other metal ions with different sizes and valences, such as potassium, magnesium, calcium, and aluminum ions can also be intercalated into 2D MXenes.[10b,109] Combining with the metallic conductivity and oxide-like surface functional groups, MXenes hold great promises for non-lithium and non-sodium batteries. Additionally, first principle simulations suggest that oxygen-terminated MXenes can deliver very high theoretical capacities for lithium, sodium, potassium, magnesium, calcium and aluminum-ion batteries (**Figure 9**a), and the formation of an additional metal layer predicted for lithium and other ions would lead to a doubling of the capacities.[9f,84a]

For instance, potassium-ion batteries (PIBs) based on 3D poly(diallyldimethylammonium chloride) modified N-rich porous carbon nanosheets/Ti_3C_2 (PDDA-NPCN/Ti_3C_2) hybrids (Figure 9b,c) delivered a high reversible capacity of 526.6 mAh g^{-1} at 0.1 A g^{-1}, which is much larger than exfoliated Ti_3C_2 (ex-Ti_3C_2) (172.3 mAh g^{-1}) and PDDA-NPCNs (387.3 mAh g^{-1}) (Figure 9d). Its rate capability and long-term stability were also excellent, showing a high reversible capacity of 191.2 mAh g^{-1} at 2 A g^{-1} and only 0.03% degradation per cycle within 2000 cycles at 1 A g^{-1} (Figure 9e,f).[14a] Most likely, this optimal electrochemical performance can be attributed to enlarged interlayer spacing, unique 3D porous interconnected conductive network and abundant utilization of active sites in electrostatically self-assembled 3D PDDA-NPCN/Ti_3C_2 hybrids. 3D MXenes also
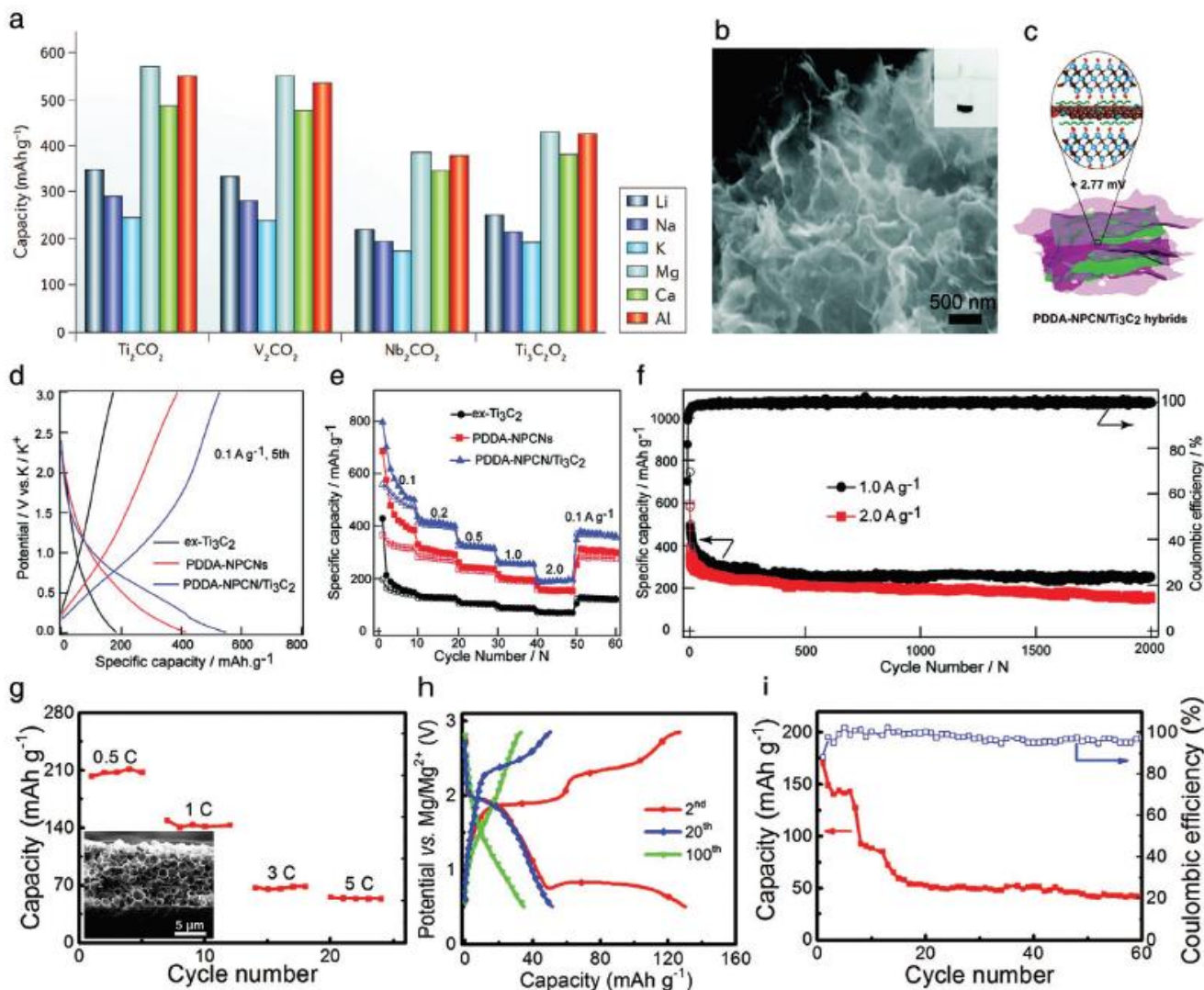
Figure 9. 3D MXene architectures for metal-ion batteries beyond lithium and sodium. a) Theoretical capacities of some oxygen terminated MXenes. Reproduced with permission.[9f] Copyright 2017, Nature Publishing Group. b) SEM image of the 3D (PDDA-NPCN/Ti_3C_2) hybrid. c) Structural schematic of the 3D PDDA-NPCN/Ti_3C_2. d) The 5th charge–discharge profiles at 0.1 A g^{-1}. e) Rate performance at different current densities. f) Long cycling performance of the 3D PDDA-NPCN/Ti_3C_2 anode at 1 and 2 A g^{-1} for 2000 cycles. Reproduced with permission.[14d] Copyright 2019, The Royal Society of Chemistry. g) Rate performance of the 3D $Ti_3C_2T_x$ film for magnesium-ion storage, inset is the cross-sectional SEM image of the 3D $Ti_3C_2T_x$ film. h) Charge-discharge curves of the 3D $Ti_3C_2T_x$ film at the 2nd, 20th, and 100th cycles at 1 C (1 C = 100 mA g^{-1}). i) Cycling profile of the 3D $Ti_3C_2T_x$ film at 1 C. Reproduced with permission.[21c] Copyright 2019, American Chemical Society.

showed promising results for magnesium-ion batteries (MIBs). Templated 3D macroporous $Ti_3C_2T_x$ films could deliver high capacities of ≈210, ≈140, and ≈55 mAh g^{-1} at 0.5 C, 1 C, and 5 C, respectively (Figure 9g).[21c] The charge-storage mechanisms for $Ti_3C_2T_x$ in MIBs system possibly combine both intercalation and conversion processes. However, the conversion-type charge storage is irreversible due to a large activation barrier to recharge Mg-containing compounds like MgO, as suggested by the disappearing of the plateau at 0.9/1.9 V after 20 cycles (Figure 9h). As a result, the capacity of 3D macroporous $Ti_3C_2T_x$ electrode was reduced from 170.5 mAh g^{-1} at the first cycle to ≈140 mAh g^{-1} during the following several cycles, and finally stabilized at ≈50 mAh g^{-1} (Figure 9i).

3.5. Lithium–Sulfur Batteries

Lithium–sulfur batteries (LSBs) have gained considerable attention in recent years because of their ultrahigh theoretical energy density (2567 Wh kg^{-1}), also abundance, low-cost and ecofriendly characteristic of the active material (i.e., sulfur).[110] Nevertheless, LSBs are still suffering from several critical issues that hinder their practical applications, such as the poor electrical conductivity of sulfur (5×10^{-30} S cm^{-1} at 25 °C),[111] the dissolution of lithium polysulfides (LPSs) (Li_2S_x, $4 \leq x \leq 8$) in organic electrolytes,[112] and the large volume expansion of cathode (≈80%) during cycling.[110c] Especially the migration of dissolved LPSs between cathode and anode, also called the internal
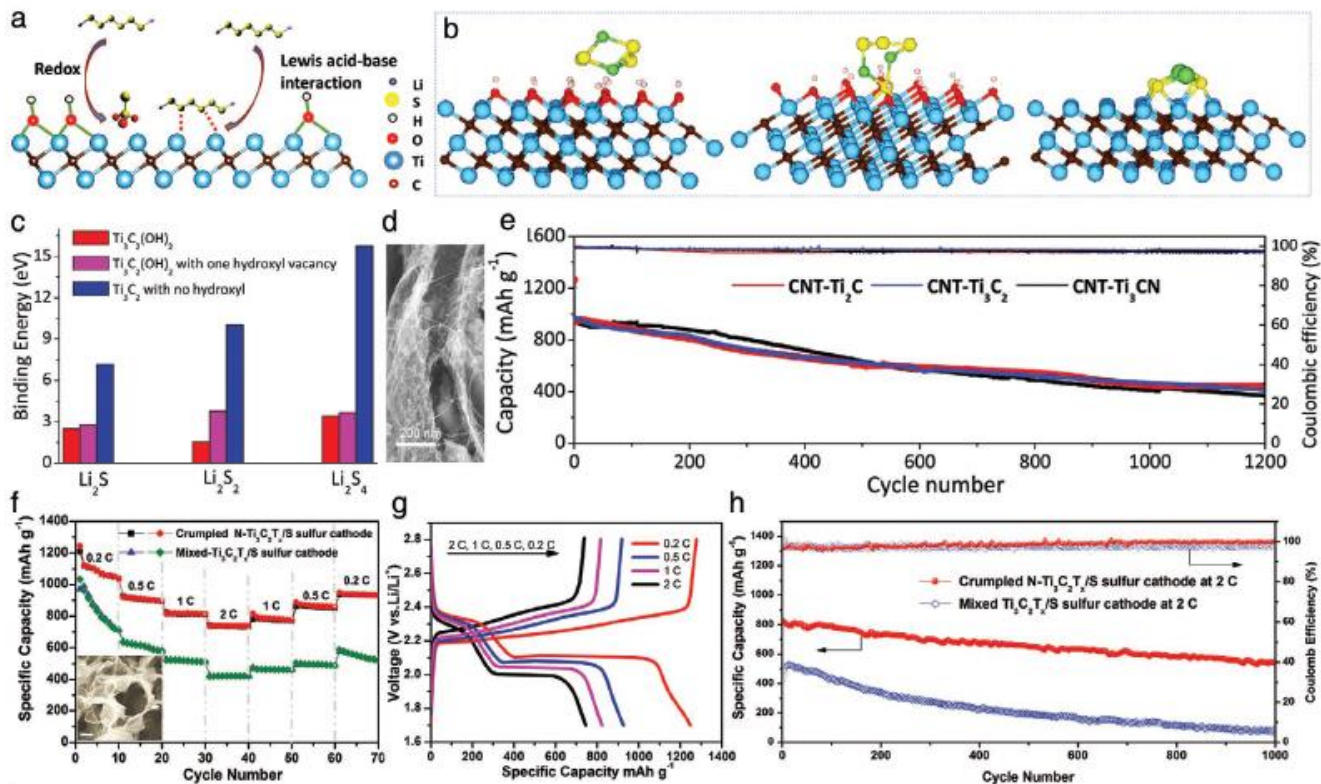
Figure 10. 3D MXene architectures for LSBs. a) Schematic illustration of two-step interaction between Ti_2CT_x MXenes and polysulfides. b) First-principles calculations for the interaction between Ti_3C_2 MXene and polysulfide Li_2S_4, showing the most stable Li_2S_4 binding geometry configuration after full relaxation on $Ti_3C_2(OH)_2$ (used to represent the pristine MXene), $Ti_3C_2(OH)_2$ with one hydroxyl vacancy and Ti_3C_2 without any surface functional groups. c) The variations of the binding energies of polysulfide molecules (Li_2S, Li_2S_2, and Li_2S_4) bonding to the respective MXenes. d) SEM image of the 3D porous CNT–Ti_3C_2. e) Long-term cycling data of three electrodes with a sulfur loading of 1.5 mg cm^{-2}, measured at a rate of C/2. Reproduced with permission.[52c] Copyright 2017, Wiley-VCH. f) Rate capability of the crumpled N-$Ti_3C_2T_x$/S and mixed-$Ti_3C_2T_x$/S at various current rates of 0.2–2 C, inset is the SEM image of crumpled N-$Ti_3C_2T_x$. g) Charge–discharge profiles of crumpled N-$Ti_3C_2T_x$/S cathode at various current rates of 0.2–2 C. h) Cycling performances of crumpled N-$Ti_3C_2T_x$/S and mixed-$Ti_3C_2T_x$/S electrodes at 2 C for 1000 cycles. Reproduced with permission.[115] Copyright 2018, WILEY-VCH.

"shuttle effect." This significantly weakens the performance of LSBs as it leads to the corrosion of Li anode and the passivation of cathode, resulting in poor Coulombic efficiency, short cycle life, significant self-discharge, large active mass loss, and obvious capacity fading.[113] To address this issue, physical adsorption approaches using high surface area materials have been widely employed.[110d,112,114] Carbons, with large effective surface area, can adsorb LPSs and effectively improve the electrical conductivity of sulfur cathodes, offering the as-fabricated LSBs very high capacities. However, the weak physical interactions between nonpolar carbon and polar polysulfide intermediates, results in irreversible loss of active materials and serious capacity fade during long-term cycling.[115] In comparison, bonding the LPSs with host materials through strong chemical interactions, such as metal-sulfur bonding[116] and polar–polar interaction,[117] appears to be a more effective strategy to suppress the polysulfide shuttle effect.

Theoretical calculations and X-ray photoelectron spectroscopy analysis suggest that MXenes can strongly bond with LPSs through dual polysulfide adsorption mode: 1) reaction of terminal hydroxyl groups with LPSs, forming thiosulfate surface species, and 2) Lewis acid–base interactions between exposed titanium atoms and additional LPSs (**Figure 10**a–c).[52c,118] As

a result, a compact S/Ti_2C composite cathode with 70 wt% sulfur loading showed a great stability with 723 mAh g^{-1} after 650 cycles at 0.5 C (1 C = 1675 mA g^{-1}), corresponding to a decay rate of 0.05% per cycle.[118]

By interweaving CNTs in between MXene layers and constructing 3D porous architectures, the electrochemical performance of the S/MXene composite cathode was further improved. This porous, electrically conductive network (Figure 10d) with high LPSs adsorption capability, led to an excellent long-term cycling performance with an ultralow fading rate of 0.043% per cycle for up to 1200 cycles (Figure 10e). This outstanding performance was resulted from the larger specific surface area and exposed active sites in CNT/MXene composites. In addition, a stable performance was also achieved for practical high mass loading electrodes, up to 5.5 mg cm^{-2} sulfur.[52c] Similarly, rGO,[40b,119] mesoporous carbon,[120] and MnO_2[121] were also employed to prevent the restacking of MXene nanosheets and offer assistance in trapping LPSs, by constructing 3D architectures. For example, freeze-dried 3D $Ti_3C_2T_x$/rGO aerogel could deliver a high capacity of 1270 mAh g^{-1} at 0.1 C, an extended cycling life up to 500 cycles with a low capacity decay rate of 0.07% per cycle, and a high areal capacity of
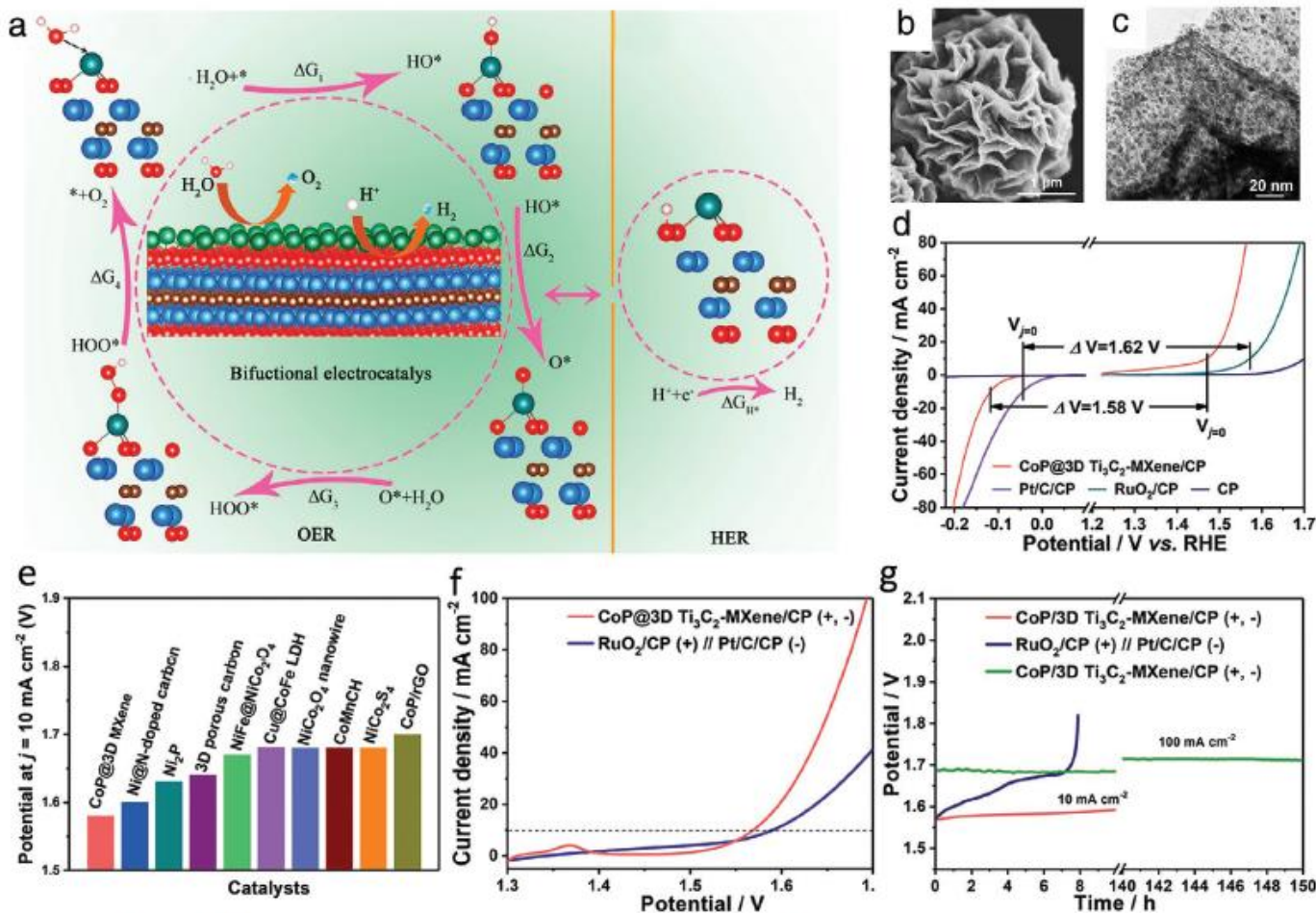
Figure 11. 3D MXene architectures for electrocatalysis. a) Schematic of the transition metal anchored on Cr_2CO_2 MXene surface as bifunctional catalyst for overall water splitting. The adsorbed states for reactions include *H, *O, *OH, and *OOH species. The blue, red, brown, green, and light pink balls represent the Cr, O, C, Ni, and H atoms, respectively. Reproduced with permission.[122b] Copyright 2018, American Chemical Society. b) SEM image of CoP@3D $Ti_3C_2T_x$–MXene architecture. c) Enlarged transmission electron microscopy image revealing the uniform dispersion of ultrafine CoP Nanoparticles on the surface of 3D MXene architecture. d) Steady-state polarization curves of various catalysts for OER and HER in 1 M KOH (CP: carbon paper). e) A comparison of CoP@3D $Ti_3C_2T_x$–MXene catalyst with the state-of-the-art nonprecious bifunctional catalysts in the voltage required to reach 10 mA cm^{-2} for overall water splitting in KOH. f) The two-electrode polarization curves at a scan rate of 10 mV s^{-1} for overall water splitting in 1 M KOH. g) Chronopotentiometric response of the devices in 1 M KOH. Reproduced with permission.[127] Copyright 2018, American Chemical Society.

5.27 mAh cm^{-2}.[40b] A self-assembled 3D MnO$_2$@Ti$_3$C$_2$ aerogel with high specific surface area and mesoporous structure, also exhibited a high active-sulfur utilization (initial discharge capacity of 1140 mAh g^{-1}), good rate capacity (reversible capacity of 615 mAh g^{-1} at 2 C), outstanding specific discharge capacity, and superior capacity retention (only 0.06% capacity decay per cycle over 500 cycles at 1 C, even at sulfur loadings up to 3.7 mg cm^{-2}).[121] Heteroatom doping was also attempted in order to strengthen the interaction between LPSs and MXene-based hosts. A 3D nitrogen-doped Ti$_3$C$_2$T$_x$ (N-Ti$_3$C$_2$T$_x$) MXene (Figure 10f inset) showed effective adsorption for LPS and thus delivered an excellent electrochemical performance (Figure 10f,g). A high capacity of ≈550 mAh g^{-1} after 1000 cycles at 2 C is by far much better than that of the mechanically-mixed Ti$_3$C$_2$T$_x$/S composites without 3D structure and modified surface (Figure 10h).[115] The electrochemical performances of 3D MXene architectures for rechargeable batteries are summarized in Table 2.

4. 3D MXene Architectures for Energy Conversion Applications

Electrocatalysis, e.g., the electrochemical splitting of water into H$_2$ and O$_2$ (**Figure 11**a), plays a key role in sustainable and clean energy conversion, which is essential for addressing the on-going climate change and fossil fuels depletion.[122] Developing high-efficiency and low-cost catalysts are of great importance for realizing the scalable application of electro-catalysis.[123] Since Mo$_2$CT$_x$ MXene was demonstrated to be an efficient electrocatalyst for HER,[124] various MXenes and MXene-based composites have been thoroughly studied as electrocatalysts through combined theoretical and experi-mental approaches.[12,13,52a,125] For example, owing to the strong covalent interactions, Pt-Mo$_2$TiC$_2$T$_x$ catalyst with single Pt atoms immobilized on Mo$_2$TiC$_2$T$_x$ was proved to exhibit a mass activity 40 times superior to the commercial Pt/C catalysts.[125a] Ti$_3$C$_2$T$_x$ MXene nanosheets also showed high

activity towards ammonium electrosynthesis, achieving a high faradic efficiency (5.78%) at an ultralow potential of −0.2 V versus RHE.[125b]

In fact, MXene meets the three key requirements for a catalyst, activity, accessibility of active sites, and conductivity. Further catalysis improvement can be considered by dispersing active materials in 3D porous structures.[126] Thus, 3D nanostructured MXenes are among the most promising candidates for catalysis operations because of their high electrical conductivity, large active surface area, abundant surface groups, and wide structural variety. For example, a capillary-forced assembled CoP@3D Ti_3C_2–MXene (Figure 11b,c) exhibited accelerated charge and mass transport through an isotopically broadened pathway, and a possible synergetic particle–MXene interaction. The CoP@3D Ti_3C_2–MXene composite delivered high electrocatalytic activity toward HER and oxygen evolution reaction (OER) in KOH (Figure 11d), resulting in superior overall-water-splitting activity and stability to the combination of precious Pt and RuO_2 catalysts, among others (Figure 11e–g).[127] In addition, other 3D MXene-based catalysis, such as N-$CoSe_2$/3D-$Ti_3C_2T_x$,[128] 3D nickel-iron/Ti_3C_2,[129] 3D Ti_3C_2/TiO_2 nanoflowers[130] and 3D FeNi-LDH/Ti_3C_2,[12] have also been developed and exhibit excellent electrocatalytic performance, demonstrating the promising potential of 3D MXenes in electrochemical energy conversion.

5. Summary and Perspectives

This review summarizes the recent progress in the preparation of 3D MXene architectures and their application in electrochemical energy storage and conversion. Various preparation methods, including template, assembly, 3D printing, and other routes, have been developed for manufacturing different kinds of 3D MXenes and their nanocomposites. Since the restacking of MXene nanosheets is effectively inhibited in these 3D architectures, more active sites are exposed for electrochemical reactions. The 3D porous structure and high electrical conductivity also offer interpenetrating pathways for highly efficient electrons and ions transport. As a result, 3D MXene architectures exhibit enhanced performance in terms of electrochemical energy storage and conversion compared to their bulk counterparts and even with other 2D materials.

Despite intensive research efforts and considerable progress to date, several key points remain to be addressed. First, the rational design and precise control over the pore morphology, including size and wall thickness. In fact, various 3D MXene architectures have been successfully synthesized, but they are all depicting unordered macroporous structures with uncontrollable wall thicknesses. Second, the poor scalability related to the production of elaborate 3D MXene architectures. Unfortunately, the mostly employed methods for constructing 3D MXene architectures still suffer from complicated procedures, limited production or toxic chemicals. Third, regarding the chemical composition, current efforts mainly focused on the hybridization of 3D MXenes with inorganic and carbon components, few organics have been introduced. Given that the diversity, multifunctionality and molecular level tailorability of organics, the integration of organics into 3D MXenes will become an important future

direction for 3D MXene architectures that leads to other new applications or breakthroughs. Fourth, the low density of 3D MXene architectures, as a result of abundant macropores, inevitably leads to low volumetric performance. Rational mechanical compression and pore structure design would be helpful for eliminating most waste void space and increasing the packing density of electrodes. Fifth, most of current 3D MXene architectures are constructed from $Ti_3C_2T_x$. Considering the diverse properties of different MXenes, the exploration of 3D MXene architectures based on other types of MXenes, such as $Mo_2TiC_2T_x$, $Nb_3C_2T_x$, and $Ta_4C_3T_x$, may lead to new developments in the field of electrochemical energy storage and conversion.

To summarize, due to their optimal physicochemical properties, 3D MXene architectures offer a plethora of new possible and exciting applications. Fast-paced developments in fabrication methods, along with the synthesis techniques, will result in greater breakthroughs and realize commercialization in the near future.

Conflict of Interest

The authors declare no conflict of interest.

[1] a) V. Nicolosi, M. Chhowalla, M. G. Kanatzidis, M. S. Strano, J. N. Coleman, Science 2013, 340, 1226419; b) K. S. Novoselov, A. K. Geim, S. V. Morozov, D. Jiang, Y. Zhang, S. V. Dubonos, I. V. Grigorieva, A. A. Firsov, Science 2004, 306, 666; c) G. Fiori, F. Bonaccorso, G. Iannaccone, T. Palacios, D. Neumaier, A. Seabaugh, S. K. Banerjee, L. Colombo, Nat. Nanotechnol. 2014, 9, 768; d) F. Xia, H. Wang, D. Xiao, M. Dubey, A. Ramasubramaniam, Nat. Photonics 2014, 8, 899; e) M. Xu, T. Liang, M. Shi, H. Chen, Chem. Rev. 2013, 113, 3766.

[2] a) Z. Cai, B. Liu, X. Zou, H.-M. Cheng, Chem. Rev. 2018, 118, 6091; b) D. Deng, K. Novoselov, Q. Fu, N. Zheng, Z. Tian, X. Bao, Nat. Nanotechnol. 2016, 11, 218; c) X. Wang, Q. Weng, Y. Yang, Y. Bando, D. Golberg, Chem. Soc. Rev. 2016, 45, 4042; d) F. Koppens, T. Mueller, P. Avouris, A. Ferrari, M. Vitiello, M. Polini, Nat. Nanotechnol. 2014, 9, 780; e) S. Z. Butler, S. M. Hollen, L. Cao, Y. Cui, J. A. Gupta, H. R. Gutierrez, T. F. Heinz, S. S. Hong, J. Huang, A. F. Ismach, E. Johnston-Halperin, M. Kuno, V. V. Plashnitsa, R. D. Robinson, R. S. Ruoff, S. Salahuddin, J. Shan, L. Shi,

M. G. Spencer, M. Terrones, W. Windl, J. E. Goldberger, *ACS Nano* **2013**, *7*, 2898.

[3] a) C. Jin, F. Lin, K. Suenaga, S. Iijima, *Phys. Rev. Lett.* **2009**, *102*, 195505; b) Y. Kubota, K. Watanabe, O. Tsuda, T. Taniguchi, *Science* **2007**, *317*, 932; c) L. Song, L. Ci, H. Lu, P. B. Sorokin, C. Jin, J. Ni, A. G. Kvashnin, D. G. Kvashnin, J. Lou, B. I. Yakobson, *Nano Lett.* **2010**, *10*, 3209.

[4] M. Chhowalla, H. S. Shin, G. Eda, L.-J. Li, K. P. Loh, H. Zhang, *Nat. Chem.* **2013**, *5*, 263.

[5] a) B. Lalmi, H. Oughaddou, H. Enriquez, A. Kara, S. Vizzini, B. Ealet, B. Aufray, *Appl. Phys. Lett.* **2010**, *97*, 223109; b) P. Vogt, P. De Padova, C. Quaresima, J. Avila, E. Frantzeskakis, M. C. Asensio, A. Resta, B. Ealet, G. Le Lay, *Phys. Rev. Lett.* **2012**, *108*, 155501.

[6] a) H. Liu, A. T. Neal, Z. Zhu, Z. Luo, X. Xu, D. Tománek, P. D. Ye, *ACS Nano* **2014**, *8*, 4033; b) L. Kou, C. Chen, S. C. Smith, *J. Phys. Chem. Lett.* **2015**, *6*, 2794.

[7] E. Bianco, S. Butler, S. Jiang, O. D. Restrepo, W. Windl, J. E. Goldberger, *ACS Nano* **2013**, *7*, 4414.

[8] J. E. ten Elshof, H. Yuan, P. Gonzalez Rodriguez, *Adv. Energy Mater.* **2016**, *6*, 1600355.

[9] a) M. Naguib, M. Kurtoglu, V. Presser, J. Lu, J. J. Niu, M. Heon, L. Hultman, Y. Gogotsi, M. W. Barsoum, *Adv. Mater.* **2011**, *23*, 4248; b) M. Naguib, O. Mashtalir, J. Carle, V. Presser, J. Lu, L. Hultman, Y. Gogotsi, M. W. Barsoum, *ACS Nano* **2012**, *6*, 1322; c) M. Naguib, V. N. Mochalin, M. W. Barsoum, Y. Gogotsi, *Adv. Mater.* **2014**, *26*, 992; d) Y. Gogotsi, B. Anasori, *ACS Nano* **2019**, *13*, 8491; e) G. Deysher, C. E. Shuck, K. Hantanasirisakul, N. C. Frey, A. C. Foucher, K. Maleski, A. Sarycheva, V. B. Shenoy, E. A. Stach, B. Anasori, *ACS Nano* **2020**, *14*, 204; f) B. Anasori, M. R. Lukatskaya, Y. Gogotsi, *Nat. Rev. Mater.* **2017**, *2*, 16098; g) M. Naguib, M. Kurtoglu, V. Presser, J. Lu, J. Niu, M. Heon, L. Hultman, Y. Gogotsi, M. W. Barsoum, *Adv. Mater.* **2011**, *23*, 4248; h) M. Alhabeb, K. Maleski, T. S. Mathis, A. Sarycheva, C. B. Hatter, S. Uzun, A. Levitt, Y. Gogotsi, *Angew. Chem., Int. Ed.* **2018**, *57*, 5444; i) C. Chen, X. Xie, B. Anasori, A. Sarycheva, T. Makaryan, M. Zhao, P. Urbankowski, L. Miao, J. Jiang, Y. Gogotsi, *Angew. Chem., Int. Ed.* **2018**, *57*, 1846; j) Z. Wu, T. Shang, Y. Deng, Y. Tao, Q.-H. Yang, *Adv. Sci.* **2020**, *7*, 1903077.

[10] a) C. J. Zhang, B. Anasori, A. Seral-Ascaso, S.-H. Park, N. McEvoy, A. Shmeliov, G. S. Duesberg, J. N. Coleman, Y. Gogotsi, V. Nicolosi, *Adv. Mater.* **2017**, *29*, 1702678; b) M. R. Lukatskaya, O. Mashtalir, C. E. Ren, Y. Dall'Agnese, P. Rozier, P. L. Taberna, M. Naguib, P. Simon, M. W. Barsoum, Y. Gogotsi, *Science* **2013**, *341*, 1502.

[11] M. R. Lukatskaya, S. Kota, Z. Lin, M.-Q. Zhao, N. Shpigel, M. D. Levi, J. Halim, P.-L. Taberna, M. W. Barsoum, P. Simon, *Nat. Energy* **2017**, *2*, 17105.

[12] M. Z. Yu, S. Zhou, Z. Y. Wang, J. J. Zhao, J. S. Qiu, *Nano Energy* **2018**, *44*, 181.

[13] X. Wu, Z. Wang, M. Yu, L. Xiu, J. Qiu, *Adv. Mater.* **2017**, *29*, 1607017.

[14] a) R. Zhao, H. Di, X. Hui, D. Zhao, R. Wang, C. Wang, L. Yin, *Energy Environ. Sci.* **2020**, *13*, 246; b) C. E. Ren, M. Q. Zhao, T. Makaryan, J. Halim, M. Boota, S. Kota, B. Anasori, M. W. Barsoum, Y. Gogotsi, *ChemElectroChem* **2016**, *3*, 689.

[15] a) K. Li, X. Wang, S. Li, P. Urbankowski, J. Li, Y. Xu, Y. Gogotsi, *Small* **2020**, *16*, 1906851; b) Q. Yun, Q. Lu, X. Zhang, C. Tan, H. Zhang, *Angew. Chem., Int. Ed.* **2018**, *57*, 626.

[16] a) C. Zhan, M. Naguib, M. Lukatskaya, P. R. Kent, Y. Gogotsi, D.-e. Jiang, *J. Phys. Chem. Lett.* **2018**, *9*, 1223; b) B. Wang, A. Zhou, F. Liu, J. Cao, L. Wang, Q. Hu, *J. Adv. Ceram.* **2018**, *7*, 237; c) G. Sharma, E. Muthuswamy, M. Naguib, Y. Gogotsi, A. Navrotsky, D. Wu, *J. Phys. Chem. C* **2017**, *121*, 15145.

[17] a) M. Alhabeb, K. Maleski, B. Anasori, P. Lelyukh, L. Clark, S. Sin, Y. Gogotsi, *Chem. Mater.* **2017**, *29*, 7633; b) X. Xiao, H. Wang, P. Urbankowski, Y. Gogotsi, *Chem. Soc. Rev.* **2018**, *47*, 8744;

c) J. Pang, R. G. Mendes, A. Bachmatiuk, L. Zhao, H. Q. Ta, T. Gemming, H. Liu, Z. Liu, M. H. Rummeli, *Chem. Soc. Rev.* **2019**, *48*, 72.

[18] M. Yu, W. Qiu, F. Wang, T. Zhai, P. Fang, X. Lu, Y. Tong, *J. Mater. Chem. A* **2015**, *3*, 15792.

[19] a) S. Han, D. Wu, S. Li, F. Zhang, X. Feng, *Adv. Mater.* **2014**, *26*, 849; b) X. Wang, J. Feng, Y. Bai, Q. Zhang, Y. Yin, *Chem. Rev.* **2016**, *116*, 10983; c) Y. Liu, J. Goebl, Y. Yin, *Chem. Soc. Rev.* **2013**, *42*, 2610.

[20] Q. Quan, X. Lin, N. Zhang, Y.-J. Xu, *Nanoscale* **2017**, *9*, 2398.

[21] a) M.-Q. Zhao, X. Xie, C. E. Ren, T. Makaryan, B. Anasori, G. Wang, Y. Gogotsi, *Adv. Mater.* **2017**, *29*, 1702410; b) X. Li, X. Yin, C. Song, M. Han, H. Xu, W. Duan, L. Cheng, L. Zhang, *Adv. Funct. Mater.* **2018**, *28*, 1803938; c) M.-Q. Zhao, C. E. Ren, M. Alhabeb, B. Anasori, M. W. Barsoum, Y. Gogotsi, *ACS Appl. Energy Mater.* **2019**, *2*, 1572; d) X. Wang, T. S. Mathis, K. Li, Z. Lin, L. Vlcek, T. Torita, N. C. Osti, C. Hatter, P. Urbankowski, A. Sarycheva, *Nat. Energy* **2019**, *4*, 241; e) M. Zhu, Y. Yue, Y. Cheng, Y. Zhang, J. Su, F. Long, X. Jiang, Y. Ma, Y. Gao, *Adv. Electron. Mater.* **2019**, *6*, 1901064.

[22] a) L. Yu, Z. Fan, Y. Shao, Z. Tian, J. Sun, Z. Liu, *Adv. Energy Mater.* **2019**, *9*, 1901839; b) Z. Fan, C. Wei, L. Yu, Z. Xia, J. Cai, Z. Tian, G. Zou, S. X. Dou, J. Sun, *ACS Nano* **2020**, *14*, 867.

[23] a) X. Xie, K. Kretschmer, B. Anasori, B. Sun, G. Wang, Y. Gogotsi, *ACS Appl. Nano Mater.* **2018**, *1*, 505; b) Q. Zhao, Q. Zhu, J. Miao, P. Zhang, P. Wan, L. He, B. Xu, *Small* **2019**, *15*, 1904293.

[24] a) Y. Tian, C. Yang, W. Que, Y. He, X. Liu, Y. Luo, X. Yin, L. B. Kong, *J. Power Sources* **2017**, *369*, 78; b) J. Guo, Y. Zhao, A. Liu, T. Ma, *Electrochim. Acta* **2019**, *305*, 164; c) M. Hu, Z. Li, H. Zhang, T. Hu, C. Zhang, Z. Wu, X. Wang, *Chem. Commun.* **2015**, *51*, 13531; d) Y. Tang, C. Yang, Y. Yang, X. Yin, W. Que, J. Zhu, *Electrochim. Acta* **2019**, *296*, 762; e) D. Song, X. Li, X.-P. Li, X. Jia, P. Min, Z.-Z. Yu, *J. Colloid Interface Sci.* **2019**, *555*, 751.

[25] X. Zhao, X.-J. Zha, J.-H. Pu, L. Bai, R.-Y. Bao, Z.-Y. Liu, M.-B. Yang, W. Yang, *J. Mater. Chem. A* **2019**, *7*, 10446.

[26] Y. Wang, J. Yang, Z. Chen, Y. Hu, *RSC Adv.* **2019**, *9*, 41038.

[27] a) Y. Yue, N. Liu, W. Liu, M. Li, Y. Ma, C. Luo, S. Wang, J. Rao, X. Hu, J. Su, Z. Zhang, Q. Huang, Y. Gao, *Nano Energy* **2018**, *50*, 79; b) X.-P. Li, Y. Li, X. Li, D. Song, P. Min, C. Hu, H.-B. Zhang, N. Koratkar, Z.-Z. Yu, *J. Colloid Interface Sci.* **2019**, *542*, 54.

[28] Q. Wang, S. Wang, X. Guo, L. Ruan, N. Wei, Y. Ma, J. Li, M. Wang, W. Li, W. Zeng, *Adv. Electron. Mater.* **2019**, *5*, 1900537.

[29] a) Z. Zhou, W. Panatdasirisuk, T. S. Mathis, B. Anasori, C. Lu, X. Zhang, Z. Liao, Y. Gogotsi, S. Yang, *Nanoscale* **2018**, *10*, 6005; b) K. Yang, F. Yin, D. Xia, H. Peng, J. Yang, W. Yuan, *Nanoscale* **2019**, *11*, 9949; c) W. Yuan, K. Yang, H. Peng, F. Li, F. Yin, *J. Mater. Chem. A* **2018**, *6*, 18116.

[30] a) R. Bian, G. He, W. Zhi, S. Xiang, T. Wang, D. Cai, *J. Mater. Chem. C* **2019**, *7*, 474; b) Q. Zhang, G. Yi, Z. Fu, H. Yu, S. Chen, X. Quan, *ACS Nano* **2019**, *13*, 13196; c) W. Bao, X. Tang, X. Guo, S. Choi, C. Wang, Y. Gogotsi, G. Wang, *Joule* **2018**, *2*, 778; d) W. Bao, C. E. Shuck, W. Zhang, X. Guo, Y. Gogotsi, G. Wang, *ACS Nano* **2019**, *13*, 11500; e) Q. Meng, Q. Jin, X. Wang, W. Lv, X. Ma, L. Li, L. Wu, H. Gao, C. Zhu, X. Zhang, *J. Alloys Compd.* **2020**, *816*, 153155; f) X. Zhang, X. Liu, S. Dong, J. Yang, Y. Liu, *Appl. Mater. Today* **2019**, *16*, 315; g) M. Han, X. Yin, K. Hantanasirisakul, X. Li, A. Iqbal, C. B. Hatter, B. Anasori, C. M. Koo, T. Torita, Y. Soda, *Adv. Opt. Mater.* **2019**, *7*, 1900267; h) X. Wu, B. Han, H.-B. Zhang, X. Xie, T. Tu, Y. Zhang, Y. Dai, R. Yang, Z.-Z. Yu, *Chem. Eng. J.* **2020**, *381*, 122622; i) H. Shi, C. J. Zhang, P. Lu, Y. Dong, P. Wen, Z.-S. Wu, *ACS Nano* **2019**, *13*, 14308.

[31] a) Y. Ma, Y. Yue, H. Zhang, F. Cheng, W. Zhao, J. Rao, S. Luo, J. Wang, X. Jiang, Z. Liu, N. Liu, Y. Gao, *ACS Nano* **2018**, *12*, 3209; b) Y. Yue, N. Liu, Y. Ma, S. Wang, W. Liu, C. Luo, H. Zhang, F. Cheng, J. Rao, X. Hu, J. Su, Y. Gao, *ACS Nano* **2018**, *12*, 4224;

c) R. Butt, A. H. Siddique, S. W. Bokhari, S. Jiang, D. Lei, X. Zhou, Z. Liu, *Int. J. Energy Res.* **2019**, *43*, 4995.

[32] a) J. Liu, H.-B. Zhang, X. Xie, R. Yang, Z. Liu, Y. Liu, Z.-Z. Yu, *Small* **2018**, *14*, 1802479; b) N.-N. Wang, H. Wang, Y.-Y. Wang, Y.-H. Wei, J.-Y. Si, A. C. Y. Yuen, J.-S. Xie, B. Yu, S.-E. Zhu, H.-D. Lu, *ACS Appl. Mater. Interfaces* **2019**, *11*, 40512.

[33] Z. Chen, Y. Hu, H. Zhuo, L. Liu, S. Jing, L. Zhong, X. Peng, R.-c. Sun, *Chem. Mater.* **2019**, *31*, 3301.

[34] P. Lin, J. Xie, Y. He, X. Lu, W. Li, J. Fang, S. Yan, L. Zhang, X. Sheng, Y. Chen, *Sol. Energy Mater. Sol. Cells* **2020**, *206*, 110229.

[35] L. Tang, X. Zhao, C. Feng, L. Bai, J. Yang, R. Bao, Z. Liu, M. Yang, W. Yang, *Sol. Energy Mater. Sol. Cells* **2019**, *203*, 110174.

[36] R. Liu, A. Zhang, J. Tang, J. Tian, W. Huang, J. Cai, C. Barrow, W. Yang, J. Liu, *Chem. - Eur. J.* **2019**, *25*, 5547.

[37] K. Zhang, G. Ying, L. Liu, F. Ma, L. Su, C. Zhang, D. Wu, X. Wang, Y. Zhou, *Materials* **2019**, *12*, 188.

[38] X. Tang, H. Liu, X. Guo, S. Wang, W. Wu, A. K. Mondal, C. Wang, G. Wang, *Mater. Chem. Front.* **2018**, *2*, 1811.

[39] a) Z. Lin, J. Liu, W. Peng, Y. Zhu, Y. Zhao, K. Jiang, M. Peng, Y. Tan, *ACS Nano* **2020**, *14*, 2109; b) Y. Deng, T. Shang, Z. Wu, Y. Tao, C. Luo, J. Liang, D. Han, R. Lyu, C. Qi, W. Lv, F. Kang, Q.-H. Yang, *Adv. Mater.* **2019**, *31*, 1902432; c) Z. Ma, X. Zhou, W. Deng, D. Lei, Z. Liu, *ACS Appl. Mater. Interfaces* **2018**, *10*, 3634.

[40] a) S. Zhao, H. B. Zhang, J. Q. Luo, Q. W. Wang, B. Xu, S. Hong, Z. Z. Yu, *ACS Nano* **2018**, *12*, 11193; b) J. Song, X. Guo, J. Zhang, Y. Chen, C. Zhang, L. Luo, F. Wang, G. Wang, *J. Mater. Chem. A* **2019**, *7*, 6507; c) X. Zhang, R. Lv, A. Wang, W. Guo, X. Liu, J. Luo, *Angew. Chem., Int. Ed.* **2018**, *57*, 15028; d) W. Ma, H. Chen, S. Hou, Z. Huang, Y. Huang, S. Xu, F. Fan, Y. Chen, *ACS Appl. Mater. Interfaces* **2019**, *11*, 25369; e) C. Yang, Q. Jiang, W. Li, H. He, L. Yang, Z. Lu, H. Huang, *Chem. Mater.* **2019**, *31*, 9277; f) Z. Wang, N. Zhang, M. Yu, J. Liu, S. Wang, J. Qiu, *J. Energy Chem.* **2019**, *37*, 183; g) X. Zhao, L.-M. Peng, C.-Y. Tang, J.-H. Pu, X.-J. Zha, K. Ke, R.-Y. Bao, M.-B. Yang, W. Yang, *Mater. Horiz.* **2020**, *7*, 855.

[41] a) L. Li, M. Zhang, X. Zhang, Z. Zhang, *J. Power Sources* **2017**, *364*, 234; b) T. Shang, Z. Lin, C. Qi, X. Liu, P. Li, Y. Tao, Z. Wu, D. Li, P. Simon, Q. H. Yang, *Adv. Funct. Mater.* **2019**, *29*, 1903960.

[42] Y. Jiang, X. Xie, Y. Chen, Y. Liu, R. Yang, G. Sui, *J. Mater. Chem. C* **2018**, *6*, 8679.

[43] X. Wang, Q. Fu, J. Wen, X. Ma, C. Zhu, X. Zhang, D. Qi, *Nanoscale* **2018**, *10*, 20828.

[44] a) S. Shi, B. Qian, X. Wu, H. Sun, H. Wang, H.-B. Zhang, Z.-Z. Yu, T. P. Russell, *Angew. Chem., Int. Ed.* **2019**, *58*, 18171; b) R. Bian, R. Lin, G. Wang, G. Lu, W. Zhi, S. Xiang, T. Wang, P. S. Clegg, D. Cai, W. Huang, *Nanoscale* **2018**, *10*, 3621.

[45] a) R. Sun, H.-B. Zhang, J. Liu, X. Xie, R. Yang, Y. Li, S. Hong, Z.-Z. Yu, *Adv. Funct. Mater.* **2017**, *27*, 1702807; b) J. Yan, C. E. Ren, K. Maleski, C. B. Hatter, B. Anasori, P. Urbankowski, A. Sarycheva, Y. Gogotsi, *Adv. Funct. Mater.* **2017**, *27*, 1701264.

[46] J. Lao, R. Lv, J. Gao, A. Wang, J. Wu, J. Luo, *ACS Nano* **2018**, *12*, 12464.

[47] V. Natu, M. Clites, E. Pomerantseva, M. W. Barsoum, *Mater. Res. Lett.* **2018**, *6*, 230.

[48] D. Zhao, M. Clites, G. Ying, S. Kota, J. Wang, V. Natu, X. Wang, E. Pomerantseva, M. Cao, M. W. Barsoum, *Chem. Commun.* **2018**, *54*, 4533.

[49] a) X. Tian, J. Jin, S. Yuan, C. K. Chua, S. B. Tor, K. Zhou, *Adv. Energy Mater.* **2017**, *7*, 1700127; b) K. Fu, Y. Yao, J. Dai, L. Hu, *Adv. Mater.* **2017**, *29*, 1603486.

[50] a) C. J. Zhang, L. McKeon, M. P. Kremer, S.-H. Park, O. Ronan, A. Seral-Ascaso, S. Barwich, C. Ó. Coileáin, N. McEvoy, H. C. Nerl, *Nat. Commun.* **2019**, *10*, 1795; b) J. Orangi, F. Hamade, V. A. Davis, M. Beidaghi, *ACS Nano* **2020**, *14*, 640.

[51] W. Yang, J. Yang, J. J. Byun, F. P. Moissinac, J. Xu, S. J. Haigh, M. Domingos, M. A. Bissett, R. A. Dryfe, S. Barg, *Adv. Mater.* **2019**, *31*, 1902725.

[52] a) Y. Fang, Z. Liu, J. Han, Z. Jin, Y. Han, F. Wang, Y. Niu, Y. Wu, Y. Xu, *Adv. Energy Mater.* **2019**, *9*, 1803406; b) S. Xu, G. Wei, J. Li, Y. Ji, N. Klyui, V. Izotov, W. Han, *Chem. Eng. J.* **2017**, *317*, 1026; c) X. Liang, Y. Rangom, C. Y. Kwok, Q. Pang, L. F. Nazar, *Adv. Mater.* **2017**, *29*, 1603040.

[53] a) T. Xu, J. M. Miszuk, Y. Zhao, H. Sun, H. Fong, *Adv. Healthcare Mater.* **2015**, *4*, 2238; b) W. Chen, S. Chen, Y. Morsi, H. El-Hamshary, M. El-Newhy, C. Fan, X. Mo, *ACS Appl. Mater. Interfaces* **2016**, *8*, 24415; c) W. E. Teo, S. Ramakrishna, *Nanotechnology* **2006**, *17*, R89.

[54] I. S. Chronakis, *J. Mater. Process. Technol.* **2005**, *167*, 283.

[55] X.-H. Qin, Y.-Q. Wan, J.-H. He, J. Zhang, J.-Y. Yu, S.-Y. Wang, *Polymer* **2004**, *45*, 6409.

[56] K. Maleski, V. N. Mochalin, Y. Gogotsi, *Chem. Mater.* **2017**, *29*, 1632.

[57] C. Jiang, C. Wu, X. Li, Y. Yao, L. Lan, F. Zhao, Z. Ye, Y. Ying, J. Ping, *Nano Energy* **2019**, *59*, 268.

[58] A. S. Levitt, M. Alhabeb, C. B. Hatter, A. Sarycheva, G. Dion, Y. Gogotsi, *J. Mater. Chem. A* **2019**, *7*, 269.

[59] W. Shao, M. Tebyetekerwa, I. Marriam, W. Li, Y. Wu, S. Peng, S. Ramakrishna, S. Yang, M. Zhu, *J. Power Sources* **2018**, *396*, 683.

[60] E. A. Mayerberger, R. M. Street, R. M. McDaniel, M. W. Barsoum, C. L. Schauer, *RSC Adv.* **2018**, *8*, 35386.

[61] E. A. Mayerberger, O. Urbanek, R. M. McDaniel, R. M. Street, M. W. Barsoum, C. L. Schauer, *J. Appl. Polym. Sci.* **2017**, *134*, 45295.

[62] X. Huang, R. Wang, T. Jiao, G. Zou, F. Zhan, J. Yin, L. Zhang, J. Zhou, Q. Peng, *ACS Omega* **2019**, *4*, 1897.

[63] a) M. Costantini, A. Barbetta, in *Functional 3D Tissue Engineering Scaffolds* (Eds: Y. Deng, J. Kuiper), Elsevier, Amsterdam **2018**, p. 127; b) P. Song, C. Zhou, H. Fan, B. Zhang, X. Pei, Y. Fan, Q. Jiang, R. Bao, Q. Yang, Z. Dong, *Composites, Part B* **2018**, *152*, 151; c) J. Hao, Y. Liao, Y. Zhong, D. Shu, C. He, S. Guo, Y. Huang, J. Zhong, L. Hu, *Carbon* **2015**, *94*, 879.

[64] J. Liu, H. B. Zhang, R. Sun, Y. Liu, Z. Liu, A. Zhou, Z. Z. Yu, *Adv. Mater.* **2017**, *29*, 1702367.

[65] P. Simon, Y. Gogotsi, *Nat. Mater.* **2008**, *7*, 845.

[66] a) C. Liu, Z. Yu, D. Neff, A. Zhamu, B. Z. Jang, *Nano Lett.* **2010**, *10*, 4863; b) R. Zhao, K. Li, R. Liu, M. Sarfraz, I. Shakir, Y. Xu, *J. Mater. Chem. A* **2017**, *5*, 19098; c) J. Chmiola, C. Largeot, P.-L. Taberna, P. Simon, Y. Gogotsi, *Science* **2010**, *328*, 480; d) D. N. Futaba, K. Hata, T. Yamada, T. Hiraoka, Y. Hayamizu, Y. Kakudate, O. Tanaike, H. Hatori, M. Yumura, S. Iijima, *Nat. Mater.* **2006**, *5*, 987; e) L. L. Zhang, X. Zhao, *Chem. Soc. Rev.* **2009**, *38*, 2520.

[67] a) G. A. Snook, P. Kao, A. S. Best, *J. Power Sources* **2011**, *196*, 1; b) K. Li, J. Liu, Y. Huang, F. Bu, Y. Xu, *J. Mater. Chem. A* **2017**, *5*, 5466; c) K. Li, Y. Huang, J. Liu, M. Sarfraz, P. O. Agboola, I. Shakir, Y. Xu, *J. Mater. Chem. A* **2018**, *6*, 1802; d) Y. Shi, L. Peng, Y. Ding, Y. Zhao, G. Yu, *Chem. Soc. Rev.* **2015**, *44*, 6684; e) Y. Song, T. Y. Liu, X. X. Xu, D. Y. Feng, Y. Li, X. X. Liu, *Adv. Funct. Mater.* **2015**, *25*, 4626; f) L. Wen, K. Li, J. Liu, Y. Huang, F. Bu, B. Zhao, Y. Xu, *RSC Adv.* **2017**, *7*, 7688.

[68] a) J. Chang, M. Jin, F. Yao, T. H. Kim, V. T. Le, H. Yue, F. Gunes, B. Li, A. Ghosh, S. Xie, *Adv. Funct. Mater.* **2013**, *23*, 5074; b) J. Yan, Z. Fan, W. Sun, G. Ning, T. Wei, Q. Zhang, R. Zhang, L. Zhi, F. Wei, *Adv. Funct. Mater.* **2012**, *22*, 2632; c) S.-J. Bao, C. M. Li, C.-X. Guo, Y. Qiao, *J. Power Sources* **2008**, *180*, 676.

[69] a) Z. Yang, J. Deng, X. Chen, J. Ren, H. Peng, *Angew. Chem.* **2013**, *125*, 13695; b) B. Anothumakkool, R. Soni, S. N. Bhange, S. Kurungot, *Energy Environ. Sci.* **2015**, *8*, 1339; c) Q. Wu, Y. Xu, Z. Yao, A. Liu, G. Shi, *ACS Nano* **2010**, *4*, 1963; d) G. Yu, L. Hu, N. Liu, H. Wang, M. Vosgueritchian, Y. Yang, Y. Cui, Z. Bao, *Nano Lett.* **2011**, *11*, 4438; e) Y. Liu, Y. Zhang, G. Ma, Z. Wang, K. Liu, H. Liu, *Electrochim. Acta* **2013**, *88*, 519; f) Z. Fan, J. Yan, T. Wei, L. Zhi, G. Ning, T. Li, F. Wei, *Adv. Funct. Mater.* **2011**, *21*, 2366.

[70] M.-Q. Zhao, C. E. Ren, Z. Ling, M. R. Lukatskaya, C. Zhang, K. L. Van Aken, M. W. Barsoum, Y. Gogotsi, *Adv. Mater.* **2015**, *27*, 339.

[71] Z. Ling, C. E. Ren, M.-Q. Zhao, J. Yang, J. M. Giammarco, J. Qiu, M. W. Barsoum, Y. Gogotsi, *Proc. Natl. Acad. Sci. USA* **2014**, *111*, 16676.

[72] M. Ghidiu, M. R. Lukatskaya, M. Q. Zhao, Y. Gogotsi, M. W. Barsoum, *Nature* **2014**, *516*, 78.

[73] J. Halim, S. Kota, M. R. Lukatskaya, M. Naguib, M.-Q. Zhao, E. J. Moon, J. Pitock, J. Nanda, S. J. May, Y. Gogotsi, M. W. Barsoum, *Adv. Funct. Mater.* **2016**, *26*, 3118.

[74] a) B. G. Choi, M. Yang, W. H. Hong, J. W. Choi, Y. S. Huh, *ACS Nano* **2012**, *6*, 4020; b) Y. Meng, K. Wang, Y. Zhang, Z. Wei, *Adv. Mater.* **2013**, *25*, 6985; c) X. Cao, Y. Shi, W. Shi, X. Rui, Q. Yan, J. Kong, H. Zhang, *Small* **2013**, *9*, 3433.

[75] a) M. F. El-Kady, M. Ihns, M. Li, J. Y. Hwang, M. F. Mousavi, L. Chaney, A. T. Lech, R. B. Kaner, *Proc. Natl. Acad. Sci. USA* **2015**, *112*, 4233; b) M. Acerce, D. Voiry, M. Chhowalla, *Nat. Nanotechnol.* **2015**, *10*, 313.

[76] a) J. R. Miller, R. Outlaw, B. Holloway, *Science* **2010**, *329*, 1637; b) Y. Yoon, K. Lee, S. Kwon, S. Seo, H. Yoo, S. Kim, Y. Shin, Y. Park, D. Kim, J.-Y. Choi, *ACS Nano* **2014**, *8*, 4580.

[77] Y. Xia, T. S. Mathis, M. Q. Zhao, B. Anasori, A. Dang, Z. Zhou, H. Cho, Y. Gogotsi, S. Yang, *Nature* **2018**, *557*, 409.

[78] X. Jian, M. He, L. Chen, M.-m. Zhang, R. Li, L.-j. Gao, F. Fu, Z.-h. Liang, *Electrochim. Acta* **2019**, *318*, 820.

[79] Y. Wang, X. Wang, X. Li, Y. Bai, H. Xiao, Y. Liu, R. Liu, G. Yuan, *Adv. Funct. Mater.* **2019**, *29*, 1900326.

[80] L. Shi, S. Lin, L. Li, W. Wu, L. Wu, H. Gao, X. Zhang, *Ceram. Int.* **2018**, *44*, 13901.

[81] Y. Wang, H. Dou, J. Wang, B. Ding, Y. Xu, Z. Chang, X. Hao, *J. Power Sources* **2016**, *327*, 221.

[82] a) Y. Huang, K. Li, G. Yang, M. F. A. Aboud, I. Shakir, Y. Xu, *Small* **2018**, *14*, 1703969; b) Y. Liu, X. Yan, Y. Yu, X. Yang, *J. Mater. Chem. A* **2015**, *3*, 20880.

[83] J. Luo, X. Tao, J. Zhang, Y. Xia, H. Huang, L. Zhang, Y. Gan, C. Liang, W. Zhang, *ACS Nano* **2016**, *10*, 2491.

[84] a) Y. Xie, Y. Dall'Agnese, M. Naguib, Y. Gogotsi, M. W. Barsoum, H. L. Zhuang, P. R. C. Kent, *ACS Nano* **2014**, *8*, 9606; b) Y. Xie, M. Naguib, V. N. Mochalin, M. W. Barsoum, Y. Gogotsi, X. Yu, K.-W. Nam, X.-Q. Yang, A. I. Kolesnikov, P. R. C. Kent, *J. Am. Chem. Soc.* **2014**, *136*, 6385.

[85] D. Sun, Q. Hu, J. Chen, X. Zhang, L. Wang, Q. Wu, A. Zhou, *ACS Appl. Mater. Interfaces* **2016**, *8*, 74.

[86] a) Q. Tang, Z. Zhou, P. Shen, *J. Am. Chem. Soc.* **2012**, *134*, 16909; b) C. Eames, M. S. Islam, *J. Am. Chem. Soc.* **2014**, *136*, 16270.

[87] a) M. Naguib, J. Come, B. Dyatkin, V. Presser, P.-L. Taberna, P. Simon, M. W. Barsoum, Y. Gogotsi, *Electrochem. Commun.* **2012**, *16*, 61; b) O. Mashtalir, M. Naguib, V. N. Mochalin, Y. Dall'Agnese, M. Heon, M. W. Barsoum, Y. Gogotsi, *Nat. Commun.* **2013**, *4*, 1716.

[88] M. Naguib, J. Halim, J. Lu, K. M. Cook, L. Hultman, Y. Gogotsi, M. W. Barsoum, *J. Am. Chem. Soc.* **2013**, *135*, 15966.

[89] C.-F. Du, Q. Liang, Y. Zheng, Y. Luo, H. Mao, Q. Yan, *ACS Appl. Mater. Interfaces* **2018**, *10*, 33779.

[90] a) J. Y. Huang, L. Zhong, C. M. Wang, J. P. Sullivan, W. Xu, L. Q. Zhang, S. X. Mao, N. S. Hudak, X. H. Liu, A. Subramanian, *Science* **2010**, *330*, 1515; b) J. S. Chen, X. W. Lou, *Small* **2013**, *9*, 1877.

[91] H. Zhang, P. Zhang, W. Zheng, W. Tian, J. Chen, Y. Zhang, Z. Sun, *Electrochim. Acta* **2018**, *285*, 94.

[92] X. Zhao, H. Xu, Z. Hui, Y. Sun, C. Yu, J. Xue, R. Zhou, L. Wang, H. Dai, Y. Zhao, *Small* **2019**, *15*, 1904255.

[93] a) S. W. Kim, D. H. Seo, X. Ma, G. Ceder, K. Kang, *Adv. Energy Mater.* **2012**, *2*, 710; b) M. D. Slater, D. Kim, E. Lee, C. S. Johnson, *Adv. Funct. Mater.* **2013**, *23*, 947; c) N. Yabuuchi, K. Kubota, M. Dahbi, S. Komaba, *Chem. Rev.* **2014**, *114*, 11636; d) J.-Y. Hwang,

S.-T. Myung, Y.-K. Sun, *Chem. Soc. Rev.* **2017**, *46*, 3529; e) Y. Huang, K. Li, J. Liu, X. Zhong, X. Duan, I. Shakir, Y. Xu, *J. Mater. Chem. A* **2017**, *5*, 2710; f) Y. Zhang, Y. Huang, G. Yang, F. Bu, K. Li, I. Shakir, Y. Xu, *ACS Appl. Mater. Interfaces* **2017**, *9*, 15549.

[94] Y. Wen, K. He, Y. Zhu, F. Han, Y. Xu, I. Matsuda, Y. Ishii, J. Cumings, C. Wang, *Nat. Commun.* **2014**, *5*, 4033.

[95] Y. Dong, Z.-S. Wu, S. Zheng, X. Wang, J. Qin, S. Wang, X. Shi, X. Bao, *ACS Nano* **2017**, *11*, 4792.

[96] X. Wang, X. Shen, Y. Gao, Z. Wang, R. Yu, L. Chen, *J. Am. Chem. Soc.* **2015**, *137*, 2715.

[97] S. Kajiyama, L. Szabova, K. Sodeyama, H. Iinuma, R. Morita, K. Gotoh, Y. Tateyama, M. Okubo, A. Yamada, *ACS Nano* **2016**, *10*, 3334.

[98] D. Er, J. Li, M. Naguib, Y. Gogotsi, V. B. Shenoy, *ACS Appl. Mater. Interfaces* **2014**, *6*, 11173.

[99] R. Wang, C. Xu, M. Du, J. Sun, L. Gao, P. Zhang, H. Yao, C. Lin, *Small* **2014**, *10*, 2260.

[100] a) X. Wang, S. Kajiyama, H. Iinuma, E. Hosono, S. Oro, I. Moriguchi, M. Okubo, A. Yamada, *Nat. Commun.* **2015**, *6*, 6544; b) X. Xie, M.-Q. Zhao, B. Anasori, K. Maleski, C. E. Ren, J. Li, B. W. Byles, E. Pomerantseva, G. Wang, Y. Gogotsi, *Nano Energy* **2016**, *26*, 513.

[101] Y. Wu, P. Nie, J. Wang, H. Dou, X. Zhang, *ACS Appl. Mater. Interfaces* **2017**, *9*, 39610.

[102] P. Lian, Y. Dong, Z.-S. Wu, S. Zheng, X. Wang, S. Wang, C. Sun, J. Qin, X. Shi, X. Bao, *Nano Energy* **2017**, *40*, 1.

[103] W. Zhang, Z.-Z. Pan, W. Lv, R. Lv, W. Shen, F. Kang, Q.-H. Yang, Y. Weng, Z.-H. Huang, *Carbon* **2019**, *153*, 625.

[104] X. Guo, X. Xie, S. Choi, Y. Zhao, H. Liu, C. Wang, S. Chang, G. Wang, *J. Mater. Chem. A* **2017**, *5*, 12445.

[105] D. Zhao, R. Zhao, S. Dong, X. Miao, Z. Zhang, C. Wang, L. Yin, *Energy Environ. Sci.* **2019**, *12*, 2422.

[106] F. Wu, Y. Jiang, Z. Ye, Y. Huang, Z. Wang, S. Li, Y. Mei, M. Xie, L. Li, R. Chen, *J. Mater. Chem. A* **2019**, *7*, 1315.

[107] J. Huang, R. Meng, L. Zu, Z. Wang, N. Feng, Z. Yang, Y. Yu, J. Yang, *Nano Energy* **2018**, *46*, 20.

[108] Y. Wu, P. Nie, J. Jiang, B. Ding, H. Dou, X. Zhang, *ChemElectroChem* **2017**, *4*, 1560.

[109] a) A. VahidMohammadi, A. Hadjikhani, S. Shahbazmohamadi, M. Beidaghi, *ACS Nano* **2017**, *11*, 11135; b) A. Byeon, M.-Q. Zhao, C. E. Ren, J. Halim, S. Kota, P. Urbankowski, B. Anasori, M. W. Barsoum, Y. Gogotsi, *ACS Appl. Mater. Interfaces* **2017**, *9*, 4296; c) M. Xu, S. Lei, J. Qi, Q. Dou, L. Liu, Y. Lu, Q. Huang, S. Shi, X. Yan, *ACS Nano* **2018**, *12*, 3733.

[110] a) Q. Pang, X. Liang, C. Y. Kwok, L. F. Nazar, *Nat. Energy* **2016**, *1*, 16132; b) P. G. Bruce, S. A. Freunberger, L. J. Hardwick, J.-M. Tarascon, *Nat. Mater.* **2012**, *11*, 19; c) Y. Dong, S. Zheng, J. Qin, X. Zhao, H. Shi, X. Wang, J. Chen, Z.-S. Wu, *ACS Nano* **2018**, *12*, 2381; d) C. Lin, C. Niu, X. Xu, K. Li, Z. Cai, Y. Zhang, X. Wang, L. Qu, Y. Xu, L. Mai, *Phys. Chem. Chem. Phys.* **2016**, *18*, 22146.

[111] G. Li, J. Sun, W. Hou, S. Jiang, Y. Huang, J. Geng, *Nat. Commun.* **2016**, *7*, 10601.

[112] X. Ji, K. T. Lee, L. F. Nazar, *Nat. Mater.* **2009**, *8*, 500.

[113] a) A. Manthiram, Y. Fu, S.-H. Chung, C. Zu, Y.-S. Su, *Chem. Rev.* **2014**, *114*, 11751; b) M. Barghamadi, A. Kapoor, C. Wen, *J. Electrochem. Soc.* **2013**, *160*, A1256.

[114] a) N. Jayaprakash, J. Shen, S. S. Moganty, A. Corona, L. A. Archer, *Angew. Chem., Int. Ed.* **2011**, *50*, 5904; b) G. Zheng, Y. Yang, J. J. Cha, S. S. Hong, Y. Cui, *Nano Lett.* **2011**, *11*, 4462; c) J. Wang, J. Yang, J. Xie, N. Xu, Y. Li, *Electrochem. Commun.* **2002**, *4*, 499; d) X. Tang, X. Guo, W. Wu, G. Wang, *Adv. Energy Mater.* **2018**, *8*, 1801897; e) W. Li, J. Liu, D. Zhao, *Nat. Rev. Mater.* **2016**, *1*, 16023.

[115] W. Bao, L. Liu, C. Wang, S. Choi, D. Wang, G. Wang, *Adv. Energy Mater.* **2018**, *8*, 1702485.

[116] a) R. Demir-Cakan, M. Morcrette, F. Nouar, C. Davoisne, T. Devic, D. Gonbeau, R. Dominko, C. Serre, G. Férey, J.-M. Tarascon, *J. Am. Chem. Soc.* **2011**, *133*, 16154; b) J. Zhou, R. Li, X. Fan, Y. Chen, R. Han, W. Li, J. Zheng, B. Wang, X. Li, *Energy Environ. Sci.* **2014**, *7*, 2715.

[117] a) Z. Lin, Z. Liu, W. Fu, N. J. Dudney, C. Liang, *Angew. Chem., Int. Ed.* **2013**, *52*, 7460; b) J. Song, T. Xu, M. L. Gordin, P. Zhu, D. Lv, Y. B. Jiang, Y. Chen, Y. Duan, D. Wang, *Adv. Funct. Mater.* **2014**, *24*, 1243; c) Z. W. Seh, W. Li, J. J. Cha, G. Zheng, Y. Yang, M. T. McDowell, P.-C. Hsu, Y. Cui, *Nat. Commun.* **2013**, *4*, 1331.

[118] X. Liang, A. Garsuch, L. F. Nazar, *Angew. Chem., Int. Ed.* **2015**, *54*, 3907.

[119] W. Bao, X. Xie, J. Xu, X. Guo, J. Song, W. Wu, D. Su, G. Wang, *Chem. - Eur. J.* **2017**, *23*, 12613.

[120] W. Bao, D. Su, W. Zhang, X. Guo, G. Wang, *Adv. Funct. Mater.* **2016**, *26*, 8746.

[121] H. Zhang, Q. Qi, P. Zhang, W. Zheng, J. Chen, A. Zhou, W. Tian, W. Zhang, Z. Sun, *ACS Appl. Energy Mater.* **2019**, *2*, 705.

[122] a) Z. W. Seh, J. Kibsgaard, C. F. Dickens, I. Chorkendorff, J. K. Nørskov, T. F. Jaramillo, *Science* **2017**, *355*, eaad4998; b) Y. Cheng, J. Dai, Y. Song, Y. Zhang, *ACS Appl. Energy Mater.* **2019**, *2*, 6851; c) H. Wang, X. Xiao, S. Liu, C.-L. Chiang, X. Kuai, C.-K. Peng, Y.-C. Lin, X. Meng, J. Zhao, J. Choi, Y.-G. Lin, J.-M. Lee, L. Gao, *J. Am. Chem. Soc.* **2019**, *141*, 18578.

[123] a) H. Wang, L. Ouyang, G. Zou, C. Sun, J. Hu, X. Xiao, L. Gao, *ACS Catal.* **2018**, *8*, 9529; b) F. Song, L. Bai, A. Moysiadou, S. Lee, C. Hu, L. Liardet, X. Hu, *J. Am. Chem. Soc.* **2018**, *140*, 7748; c) Z. Lu, G. Chen, S. Siahrostami, Z. Chen, K. Liu, J. Xie, L. Liao, T. Wu, D. Lin, Y. Liu, *Nat. Catal.* **2018**, *1*, 156;

d) Z. Weng, Y. Wu, M. Wang, J. Jiang, K. Yang, S. Huo, X.-F. Wang, Q. Ma, G. W. Brudvig, V. S. Batista, *Nat. Commun.* **2018**, *9*, 415; e) S. L. Foster, S. I. P. Bakovic, R. D. Duda, S. Maheshwari, R. D. Milton, S. D. Minteer, M. J. Janik, J. N. Renner, L. F. Greenlee, *Nat. Catal.* **2018**, *1*, 490.

[124] Z. W. Seh, K. D. Fredrickson, B. Anasori, J. Kibsgaard, A. L. Strickler, M. R. Lukatskaya, Y. Gogotsi, T. F. Jaramillo, A. Vojvodic, *ACS Energy Lett.* **2016**, *1*, 589.

[125] a) J. Zhang, Y. Zhao, X. Guo, C. Chen, C.-L. Dong, R.-S. Liu, C.-P. Han, Y. Li, Y. Gogotsi, G. Wang, *Nat. Catal.* **2018**, *1*, 985; b) Y. Luo, G.-F. Chen, L. Ding, X. Chen, L.-X. Ding, H. Wang, *Joule* **2019**, *3*, 279; c) J. Chen, X. Yuan, F. Lyu, Q. Zhong, H. Hu, Q. Pan, Q. Zhang, *J. Mater. Chem. A* **2019**, *7*, 1281; d) D. Zhao, Z. Chen, W. Yang, S. Liu, X. Zhang, Y. Yu, W.-C. Cheong, L. Zheng, F. Ren, G. Ying, *J. Am. Chem. Soc.* **2019**, *141*, 4086; e) H. Wang, Y. Lin, S. Liu, J. Li, L. Bu, J. Chen, X. Xiao, J.-H. Choi, L. Gao, J.-M. Lee, *J. Mater. Chem. A* **2020**, *8*, 7109.

[126] a) G. Fu, X. Yan, Y. Chen, L. Xu, D. Sun, J. M. Lee, Y. Tang, *Adv. Mater.* **2018**, *30*, 1704609; b) H. Wang, Y. Cao, G. Zou, Q. Yi, J. Guo, L. Gao, *ACS Appl. Mater. Interfaces* **2016**, *9*, 60; c) J. Lai, A. Nsabimana, R. Luque, G. Xu, *Joule* **2018**, *2*, 76.

[127] L. Xiu, Z. Wang, M. Yu, X. Wu, J. Qiu, *ACS Nano* **2018**, *12*, 8017.

[128] Z. Zeng, G. Fu, H. B. Yang, Y. Yan, J. Chen, Z. Yu, J. Gao, L. Y. Gan, B. Liu, P. Chen, *ACS Mater. Lett.* **2019**, *1*, 432.

[129] M. Yu, Z. Wang, J. Liu, F. Sun, P. Yang, J. Qiu, *Nano Energy* **2019**, *63*, 103880.

[130] Y. Li, X. Deng, J. Tian, Z. Liang, H. Cui, *Appl. Mater. Today* **2018**, *13*, 217.